

Review

Titanium Dioxide Nanoparticles Doped with Iron for Water Treatment via Photocatalysis: A Review

Domenico Rosa¹, Nigar Abbasova² and Luca Di Palma^{1,*} 

¹ Department of Chemical Engineering Materials Environment, Sapienza-Università di Roma, Via Eudossiana 18, 00184 Roma, Italy; domenico.rosa@uniroma1.it

² Department of Ecology, Azerbaijan University of Architecture and Construction, AZ1073 Baku, Azerbaijan; nigar.abbasova.bdu@gmail.com

* Correspondence: luca.dipalma@uniroma1.it; Tel.: +39-06-44585571

Abstract: Iron-doped titanium dioxide nanoparticles are widely employed for photocatalytic applications under visible light due to their promising performance. Nevertheless, the manufacturing process, the role of Fe³⁺ ions within the crystal lattice of titanium dioxide, and their impact on operational parameters are still a subject of controversy. Based on these assumptions, the primary objective of this review is to delineate the role of iron, ascertain the optimal quantity, and elucidate its influence on the main photocatalysis parameters, including nanoparticle size, band gap, surface area, anatase–rutile transition, and point of zero charge. Moreover, an optimized synthesis method based on comprehensive data and insights from the existing literature is proposed, focusing exclusively on iron-doped titanium oxide while excluding other dopant variants.

Keywords: titanium dioxide; doping; iron; photocatalysis; nanoparticles



Citation: Rosa, D.; Abbasova, N.; Di Palma, L. Titanium Dioxide Nanoparticles Doped with Iron for Water Treatment via Photocatalysis: A Review. *Nanomaterials* **2024**, *14*, 293. <https://doi.org/10.3390/nano14030293>

Received: 16 December 2023

Revised: 27 January 2024

Accepted: 29 January 2024

Published: 31 January 2024



Copyright: © 2024 by the authors. Licensee MDPI, Basel, Switzerland. This article is an open access article distributed under the terms and conditions of the Creative Commons Attribution (CC BY) license (<https://creativecommons.org/licenses/by/4.0/>).

1. Introduction

Heterogeneous photocatalysis, using semiconductor nanoparticles, is a promising technology for the removal of bio-refractory substances from contaminated water [1]. The development of nanostructured photocatalysts with enhanced and implementable structural, morphological, and electronic properties [2,3] proved to be effective in the treatment of industrial wastewater.

The efficacy of heterogeneous photocatalysis lies in the ability to harness sunlight or alternative light sources to activate catalytic processes capable of removing contaminants from water [4–7]. The semiconductors exhibit a valence band (VB) filled with electrons alongside a conduction band (CB) characterized by higher energy and an absence of electrons, establishing a well-defined band gap. Heterogeneous photocatalysis employed for water decontamination from organic substances involves the absorption of light with a specific wavelength by the photocatalyst. This process induces the excitation of electrons, facilitating their transition from the valence band to the conduction band of the photocatalyst. Consequently, this electron movement generates positive holes (h_{VB}^+) within the catalyst's VB, possessing a potent oxidative potential. These positive holes effectively reduce adsorbed H₂O molecules, producing free hydroxyl radicals OH, while electrons (e_{CB}^-) in the CB, notwithstanding their lower reduction potential compared to the oxidation potential of positive holes [8], are caught by oxygen molecules, leading to the formation of the superoxide radical anion O₂^{•-}. Free hydroxyl radicals stand out as powerful oxidizing agents, with an oxidation potential of 2.80 V: they can mineralize any organic compound adsorbed on the particle surface to yield water and carbon dioxide [4,5,9]. The direct oxidation effect of organic compounds by positive holes has also been hypothesized (any species with unpaired electrons or conjugated π bonds can be subject to oxidation by photogenerated positive holes) [4,10].

Surface OH groups actively take part in the photodegradation process by acting as trapping sites for $h\nu_{VB}^+$, leading to the formation of highly reactive hydroxide radicals. Alternatively, these groups may facilitate the absorption of substrate molecules. Figure 1 provides a schematic representation of the photochemical activation of titanium dioxide and the consequent formation of hydroxyl radicals.

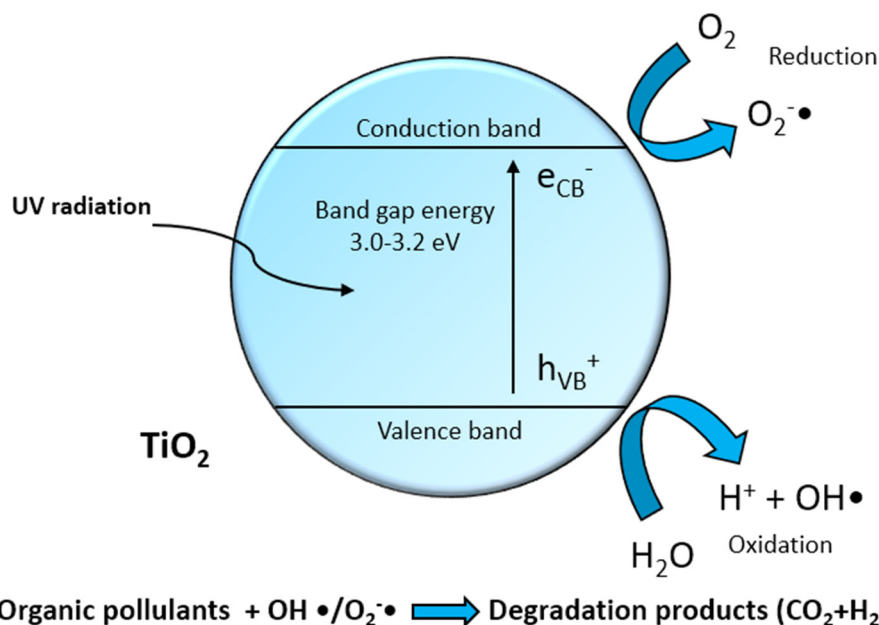


Figure 1. Schematic representation of the photochemical activation of titanium dioxide and the formation of radical species responsible for the oxidative degradation of organic pollutants.

Despite considerable efforts devoted to the investigation of photocatalytic mechanisms, the practical implementation of photocatalysis at the industrial scale remains circumscribed. The main issue limiting the transition from laboratory experimentation to large-scale application is the lack of facile and environmentally sustainable methodologies for the large-scale production of high-performance photocatalysts under visible light [11].

2. Advanced Photocatalyst

Photocatalytic materials have gained considerable interest due to their numerous applications. Through appropriate modifications, these materials can effectively overcome limitations in process efficiency [12]—hence the term “advanced catalysts”.

Their great advantage is that they can harness solar radiation. For photocatalysts such as titanium dioxide (titania, TiO₂), the most exhaustive scrutiny has been carried out [13–15] due to its cost-effectiveness [16], stability [17,18], widespread availability, and heightened activity [9,19]. A modification is essential to enhance its photochemical and adsorptive performances, especially to be active under visible light [13,20]. The primary drawback of titania is that its activity is only limited to UV radiation ($\lambda \leq 387$ nm) due to its wide bandgap (3.2 eV) [21]. Only UV photons have sufficient energy to overcome this bandgap, thus promoting photocatalysis [20]. However, titania possesses a high rate of recombination of photogenerated electron-hole pairs, significantly limiting achievable quantum yield [22].

Consequently, doping titania nanoparticles with heteroatoms to reduce the bandgap, shifting the absorption edge towards longer wavelengths, has become a common practice [23]. This modification allows the photocatalyst to be active under visible light, minimizing charge recombination and achieving the ideal nanoscale size for photocatalytic applications [22]. It is widely accepted that a lower recombination rate strongly improves photocatalytic efficiency [23].

Among potential heteroatoms, iron is highly favored for doping titania [24,25], as shown in Figure 2, due to its cost-effectiveness [26] and efficacy. Additionally, its atomic radius, similar to titanium (0.61 Å for Ti^{4+} hexacoordinated and 0.55 Å for Fe^{3+} hexacoordinated) [27], facilitates the simple substitution of iron into the crystalline lattice of titanium [28,29]. While other authors may report slightly different values, they remain closely comparable, such as 0.645 Å for Fe^{3+} and 0.604 Å for Ti^{4+} [30,31] or 0.64 Å for Fe^{3+} and 0.68 Å for Ti^{4+} [32,33].

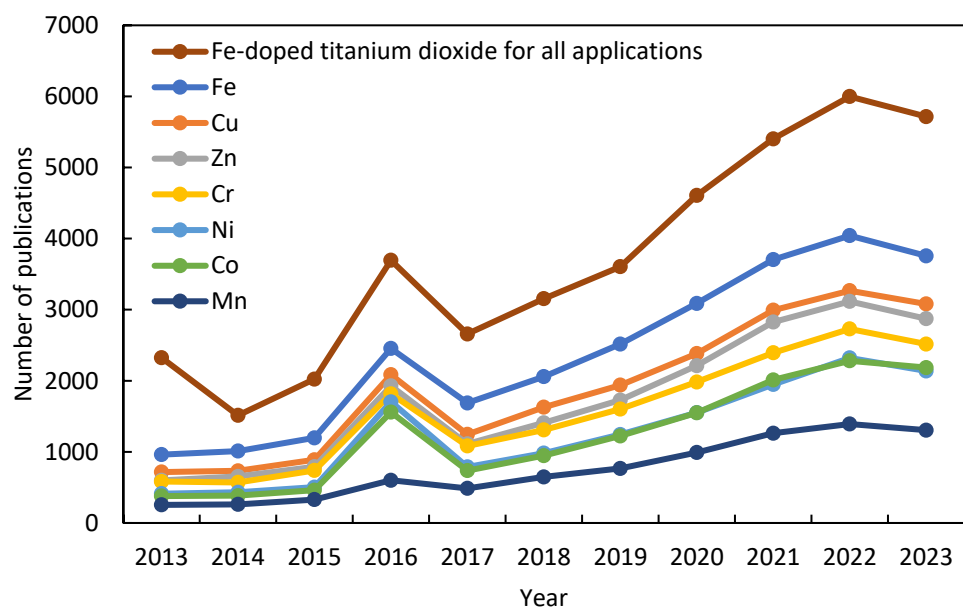


Figure 2. Number of publications on doped titanium dioxide with different transition metals for photocatalytic applications.

Figure 2 shows the number of publications related to various transition metals, including Fe, Cu, Zn, Cr, Ni, Co, and Mn, particularly in the framework of photocatalysis processes employing titanium dioxide. Furthermore, it also provides the total number of publications associated with iron-doped titania across all applications. Most of the publications on iron-doped titania are focused on its utilization in photocatalysis, constituting over half of all studies on iron-doped titania. Indeed, in 2023, there were 5716 publications on iron-doped titania, with 3757 exclusively dedicated to photocatalysis, representing 66% of all publications on iron-doped titania.

The extensive literature on iron-doped titania for photocatalysis purposes underscores its significance and appeal within the scientific community. This trend not only highlights the prevalence of iron-doped titania in photocatalytic applications but also shows its comparative advantage over alternative transition metal dopants, especially in the context of water treatment and environmental remediation.

Understanding the pivotal role of iron (Fe^{3+}) in the improvement of titania photocatalytic properties requires examination of key photocatalysis steps: (a) the photogeneration of positive hole–electron pairs, necessitating trapped/separated to prevent recombination; (b) reduction and oxidation reactions involving distinct electrons and holes interacting with appropriately adsorbed species; and (c) the progression of intermediates, desorption of products, and surface reconstruction. Iron predominantly influences steps (a) and (b) in a complex manner, demanding comprehensive exploration and discussion for optimizing the photocatalytic process [34].

It is worth emphasizing that the concept of doping is sometimes interpreted literally as the integration of isolated heteroatoms (in this case, Fe^{3+}) into a solid solution within the TiO_2 framework. However, it is commonly used to describe the deposition of small oxide particles or, more generally, a secondary phase (e.g., Fe_2O_3) onto the surface of TiO_2 .

Nonetheless, the mechanism for enhancing the photochemical response of TiO_2 differs significantly between surface-deposited or doped $\text{Fe}^{3+}/\text{TiO}_2$ or $\text{Fe}_2\text{O}_3/\text{TiO}_2$. In the former case, a reduction in the bandgap of the photocatalytic semiconductor occurs, while in the latter, a charge transfer to TiO_2 from the deposited oxide is realized, known as coupling [35].

However, as discussed more comprehensively in this review, distinguishing between these mechanisms can sometimes be challenging. Nevertheless, it is crucial to do so to justify the occasionally conflicting properties of the materials; indeed, the catalytic role during photooxidation processes remains controversial due to the significant structural modifications it can induce in the photocatalyst [36]. These alterations concerning nanoparticle size, the anatase-to-rutile phase transition, bandgap, surface properties, etc., are often interrelated and can either enhance or diminish photocatalytic performance [37–39]. For instance, Fe^{3+} cations are thought to act as scavengers for photogenerated electrons during the photocatalytic process in the titania structure [40]. However, discrepancies emerge concerning their impact on enhancing electron-hole recombination properties [23]. Some authors propose that Fe^{3+} serves as a trapping site for both electrons and positive holes, especially at high concentrations [41]. Conversely, other studies show that Fe^{3+} exclusively traps positive holes, with electrons being captured by surface Ti^{4+} [42], or that it promotes charge separation [23].

Li X. et al. (2003) found that Fe^{3+} can trap photogenerated charges at different sites simultaneously. Positive hole trapping is specifically linked to surface Fe^{3+} , whereas electron trapping is associated with bulk Fe^{3+} [43].

In general, achieving optimal photocatalytic properties typically involves doping at a relatively low level, usually below 1% [22]. However, the optimal dosage depends on nanoparticle size, diminishing as particle size increases. This trend arises because, in larger particles, charge recombination predominantly occurs in the bulk, whereas in smaller particles, it primarily takes place on the surface [42]. This phenomenon is linked to the recombination process dynamics, which can be associated with the distance between dopant cations in the titania structure [44]. Furthermore, changes in surface properties induced by doping can significantly contribute to explaining the photocatalytic performance of the system. The photocatalytic behavior of a material is determined by various physical, chemical, and electronic parameters that are often challenging to correlate. Photoactivity results from a balance of these factors, some of which frequently play conflicting roles [45].

To enhance photocatalytic performance, it is crucial to carry out a thorough investigation into how the quantity of iron affects the properties of the photocatalyst and, consequently, its photocatalytic activity. This relationship is intimately linked to morphological properties, as the photocatalytic activity is intricately correlated with these characteristics [29,46].

3. Modification of Titanium Dioxide by Iron

3.1. The Size of Nanoparticles

Titanium dioxide nanoparticles exhibit a spherical morphology [47,48], with their sizes dependent on the synthesis method employed. Common methods include sol-gel, co-precipitation, and hydrothermal approaches, with synthesis temperature also impacting nanoparticle sizes [29].

Nanoparticle size holds significant importance for catalysis, influencing the specific surface area of a catalyst. Smaller particle sizes enhance the number of specific active surface sites, thereby promoting charge carrier transfer in photocatalysis. However, Z. Zhang et al. (1998) noted that photocatalytic efficiency does not monotonically increase with decreasing particle size. An optimal size of approximately 10 nm was identified for pure nanocrystalline TiO_2 photocatalyst in the liquid-phase decomposition of chloroform due to the antagonistic effect of increased surface recombination of the positive hole-electron pair [42]. C. Almquist (2002) observed a similar phenomenon, noting significant variation in photocatalytic performance below 30 nm due to reduced likelihood of charge recombination, with an optimal size of approximately 25 nm [49]. For particles exceeding

this value, the available surface area for redox reactions diminishes as particle size increases. The introduction of iron, typically in the form of iron ions (e.g., Fe^{3+}), reduces the size of titanium dioxide nanoparticles [50], as depicted in Figure 3.

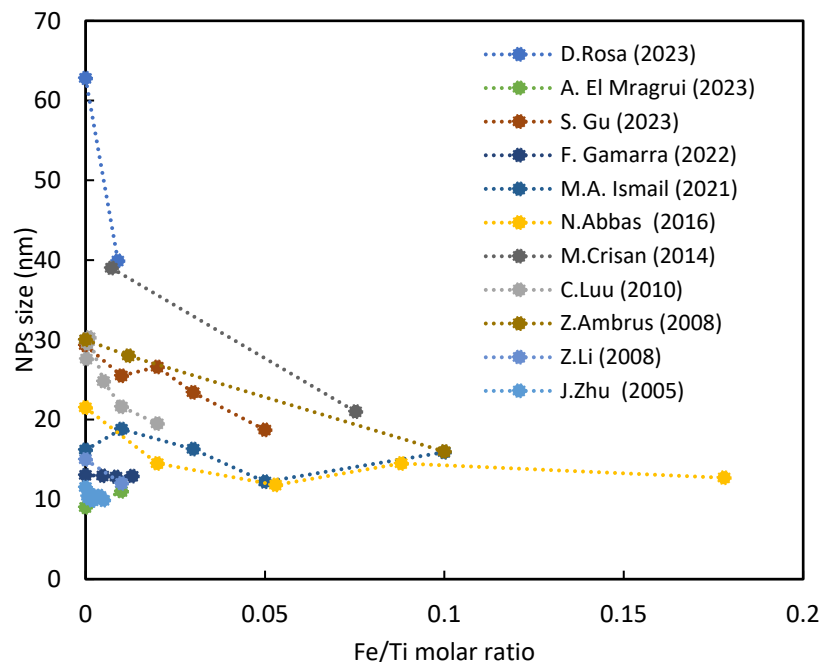


Figure 3. Size of TiO_2 nanoparticles as the amount of iron used for different syntheses [38,48,51–59].

For instance, I. Mwangi et al. (2021) reported an average diameter reduction from 13.7 nm for pure titania to 10.8 nm for iron-doped samples [47]. Similarly, Z. Ambrus et al. (2008) observed a decrease in nanoparticle size from 30 nm to 16 nm with an increase in iron content to 10%. Additionally, a progressive distortion in the nanoparticle shape, developing a more elongated form, was noted [54].

In our earlier investigation [48], we observed that nanoparticle sizes decreased from 62.8 nm to 39.9 nm upon the addition of iron to titania. Iron exerts a crystal growth suppression effect on TiO_2 , hindering particle contact and inhibiting crystal growth during heat treatment [6]. Given the slightly smaller radius of Fe^{3+} compared to the channels along the c-axis of pure TiO_2 (0.77 nm), Fe^{3+} may preferentially diffuse along the c-axis [60], substituting for Ti^{4+} in the TiO_2 lattice and causing lattice expansion due to elongation of the tetragonal cell parameter [22]. This leads to lattice deformation [38], impeding grain growth. An increase in iron content substantially alters the morphology of TiO_2 nanoparticles, causing them to lose their characteristic spherical shape and appear more agglomerated, although low iron levels have a minimal impact on morphology [61].

N. Abbas et al. (2016) reported that in samples with high iron content (35%), fine granular nanostructures became larger and more dispersed, as shown in SEM images (Figure 4).

The crystallite size increased from 21.5 to 62.1 nm, and the shape changed to a mix of spherical nanoparticles and rod-shaped structures with a length of approximately 84 nm [56] as lighted with red lines.

In summary, the morphology of titanium dioxide nanoparticles is significantly influenced by iron content, impacting their dimensions. Specifically, the addition of iron reduces both crystallites' [55] and nanoparticles' [52] sizes. This alteration is often accompanied, although not universally, by an increase in specific surface area. Beyond a certain threshold (around 10%, corresponding to a Fe/Ti ratio of 0.1), the reverse process occurs, leading to nanoparticle enlargement, likely induced by the transformation of anatase to rutile activated by iron [62]. In any case, iron contributes to rendering the nanoparticles more heterogeneous, causing them to deviate from their characteristic spherical shape.

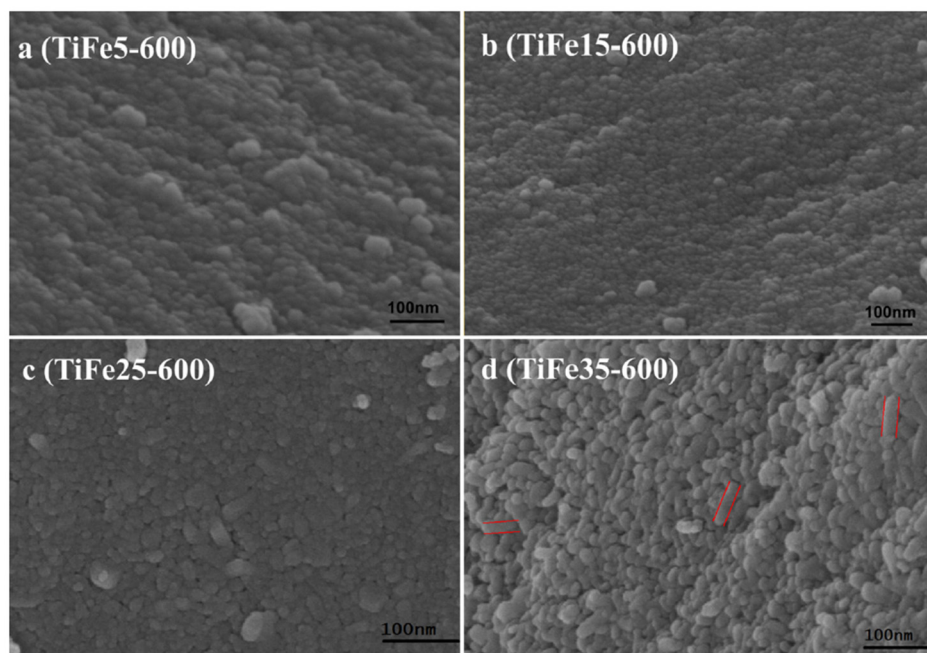


Figure 4. SEM micrography of based-TiO₂ samples doped with different amounts of iron: (a) 5%, (b) 15%, (c) 25%, (d) 35% [56].

3.2. Band Gap of Semiconductor

The incorporation of heteroatoms into the crystal structure of semiconductors, such as titanium dioxide, has the potential to decrease their band gap [63]. This is particularly evident when iron is integrated into the lattice of titania. Absorption below 380 nm (approximately 3.1 eV) is associated with the intrinsic band gap absorption of pure TiO₂ [64] (3.0 eV for the rutile phase and 3.2 eV for the anatase phase [41]). Iron doping induces absorption in the visible region, typically at 400 and 500 nm, intensifying with increasing iron content. These absorptions are linked to the excitation of 3d electrons of Fe³⁺ ions into the conduction band of TiO₂ (charge transfer transition) [65], resulting in a band at around 400 nm [22]. Iron does not impact the valence band of TiO₂ [45]. For higher iron concentrations, an additional band around 500 nm is observed, possibly due to the d–d transition of Fe³⁺ [38,66] or the charge transfer transition between interacting iron ions (2Fe³⁺ → Fe⁴⁺ + Fe²⁺) [22], with the maximum interaction occurring at approximately 1.5%.

Furthermore, iron induces the formation of structural defects, including oxygen vacancies [44]. Oxygen vacancy formation allows electrons to migrate from O 2p states in the valence band to Ti 3d states in the conduction band. Ti³⁺ states, produced by trapping electrons in defective sites, accumulate and reflect the number of defect sites [44]. Each Ti atom surrounding the removed oxygen can capture one of these electrons, forming Ti³⁺-related defect states within the bandgap, reducing the conduction band [44]. Ti³⁺ sites, increasing with decreasing nanoparticle size, serve as photocatalytically active sites and behave as coordinatively unsaturated ions. Therefore, their study, particularly in photooxidation and photocatalysis, deserves special attention [67].

The introduction of iron into the crystalline structure of titania significantly reduces the band gap (Figure 5). Even minor amounts of iron (up to a molar ratio of Fe/Ti of 0.1) drastically reduced the band gap from the 3.2 eV of pure titania to approximately 2.1–2.5 eV [6]. These values make the catalyst active under visible radiation [40], and the reduction in the band gap is due to the formation of the Fe–O–Ti bond in the crystal lattice of TiO₂ [51].

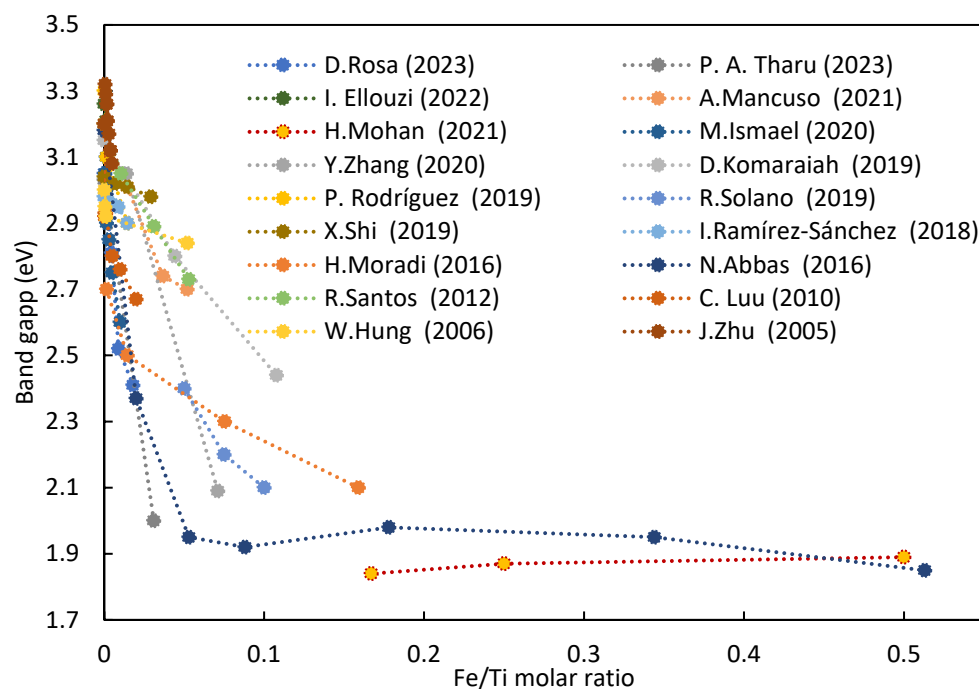


Figure 5. Band gap of titanium oxide doped with iron at varying Fe/Ti ratio [6,31,38,48,51,56,61,68–78].

Beyond a molar ratio of Fe/Ti of 0.1, a stabilization of the band gap is observed around approximately 1.9–2.1 eV, approaching the band gap value of hematite. This implies that limited quantities of iron (<10%) are required to reduce the band gap. Higher quantities do not induce a drastic decrease because iron, beyond this percentage, is no longer effectively incorporated into the crystal lattice of titania, surpassing the solubility limit of iron in titania. Excess iron tends to form a separate phase on the surface of titania, primarily as hematite (α -Fe₂O₃) [31,61], goethite (α -FeOOH) [54], ilmenite (FeTiO₃) [35], or Fe₂TiO₅ (pseudobrookite) [29,34], especially favored at high calcination temperatures [38] (800–1000 °C [29]). The coexistence of multiple phases cannot be excluded, as observed by our previous work [48] with 2% iron loading. Notably, iron exhibits a higher tendency than other transition metals (Co, Cr, Cu, and Mo) to form separate phases as iron oxide [45]. Attention is required for the segregation of surface iron, as Fe₂TiO₅ and Fe₂O₃, despite possessing a reduced band gap (2.18 eV [29] and 2.00–2.20 eV [32], respectively), exhibit low photocatalytic activity and could occupy active sites dedicated to the adsorption of contaminants and photocatalytic degradation. Therefore, meticulous control of the dopant quantity and distribution is crucial.

Several authors have reported a solubility limit of around 1% (for anatase) using conventional doping techniques [22,36,43,63]. For instance, D. Cordischi et al. (1985) found a Fe solubility of about 1% in anatase using wet preparation techniques, such as co-precipitation followed by high-temperature calcination. The solubility in rutile was only 0.1% (Fe/Ti 0.001) [34]. Iron is less soluble in rutile than in anatase due to the latter's symmetric nature, resulting in additional tunnels with larger volumes. These tunnels can accommodate cations or anions of significant dimensions introduced during crystal synthesis [79], contributing to greater solubility in anatase [29,37].

Li X. et al. (2003) observed a solubility limit of 1 at. % Fe in anatase prepared by a sol-gel process followed by annealing at 450 °C for 2 h [43]. Z. Zhang et al. (1998) reported that up to a 1% iron content in TiO₂ using the sol-gel method followed by hydrothermal treatment did not result in secondary phases [42]. Litter M. (1996) noted that iron initially present on the surface diffuses into the bulk, producing a solid solution. Samples containing up to 1% Fe substitutional solid solutions with dispersed Fe³⁺ in the TiO₂ lattice. Higher iron contents host excess iron in the form of tiny particles or small aggregates of iron oxides (hematite) and/or mixed oxides (Fe₂TiO₅) on the surface of the solid solution particles [29].

Even with less conventional techniques like the solid-state method, a separate iron phase was observed at 1% iron [48]. A more in-depth study revealed that approximately 10% of the introduced iron formed the segregated phase, with the remaining fraction effectively incorporated into the TiO₂ lattice [80].

W. Teoh (2007) observed iron segregation at Fe/Ti ratios of 0.05, notably higher than in previously reported studies, due to the extreme conditions of doping through flame spray pyrolysis [27]. Z. Wang et al. (2001), using the same technique, demonstrated the formation of the Fe phase at a Fe/Ti ratio of 0.10 [81]. Flame spray pyrolysis (FSP) may yield a higher solubility limit of Fe in TiO₂ compared to conventional techniques.

Solubility is also influenced by the type of TiO₂ and its predisposition to incorporate iron. Using Degussa P25, the iron-segregated phase formed at Fe/Ti ratios as low as 0.005, consistent with the observed band gap [48]. The reduction in band gap was less pronounced, indicating that Degussa P25 did not incorporate Fe ions into its lattice, resulting in fewer bonds responsible for reducing the Fe–O–Ti band gap.

This phenomenon could be due to the homemade titania having more structural defects compared to Degussa P25, facilitating greater ease for Fe³⁺ ions to diffuse into the crystalline lattice. This resulted in a more significant decrease in the band gap [60]. Another critical factor influencing diffusion is the calcination temperature during synthesis. Elevated temperatures (above 300 °C, with a recommended range of 600–700 °C) promote the diffusion of iron into the crystalline lattice of titania [60]. This is crucial for preventing non-uniform diffusion, primarily near the catalyst's surface, and facilitating diffusion towards the center.

In addition to calcination temperature, the doping strategy also influences diffusion. For instance, Sonia J. (1991) demonstrated that samples prepared via co-precipitation allowed for less iron diffusion into the lattice compared to the impregnation method [36].

In summary, the solubility limit of iron in the TiO₂ structure is influenced by doping strategy, material characteristics (such as the presence of structural defects), and synthesis methodology. Generally, the solubility limit is around the Fe/Ti ratio of 0.01. However, a significant reduction in band gap occurs up to Fe/Ti ratios of 0.1. This suggests that the segregated iron on the photocatalyst surface also contributes to the band gap reduction [35], likely due to the formation of Fe–O–Ti bonds at the heterojunction of the two distinct phases. However, this does not consistently translate to improved photocatalytic performance.

3.3. Surface Area

The presence of low iron concentration inhibits the growth of the titanium dioxide crystalline lattice [82,83], resulting in smaller grain size (pore) and increased surface area, which is beneficial for photocatalysis by enhancing contaminant adsorption, especially in mesoporous structures, providing more active sites for photocatalytic reactions [49]. For instance, J. Zhu et al. (2006) observed a rise in the specific surface area of TiO₂ nanoparticles with 0.5% iron from 140 to 159 m²/g [38]. Similarly, C. Almquist (2002) reported an increase in surface area at an iron content of 0.5% from 69 m²/g for the pure TiO₂ sample to 120 m²/g [49].

N. Jamalludin (2011) observed an increase in titania surface area with low iron content; pure TiO₂ exhibited 43 m²/g, while 0.4 mol % Fe³⁺ incorporation increased the surface area to 74 m²/g [84], reaching 85 m²/g at 0.8 mol % Fe³⁺. Beyond 1.0 mol % Fe³⁺, the surface area decreased from 85 to 73 m²/g.

Careful consideration of iron concentration is crucial, as excessive iron, beyond the solubility limit, may deposit as oxide [34], causing pore blockage [74] and decreasing surface area [69,85].

Shi X. (2019) observed a decrease in surface area from 120 to 107 m²/g with an increase in iron concentration from 0.5 to 2.0%. Additionally, the pore volume reduced from 0.26 to 0.21 cm³/g, and the average diameter decreased from 10.8 to 10.5 nm [74].

I. Ganesh et al. (2012) experienced an increase in surface area from 23.25 m²/g to 65.92 m²/g with 0.1% weight of Fe [86], but a gradual decrease with increasing concen-

tration, reaching 48.82 m²/g at 10% due to the pore blockage of the support by metallic oxides [45]. Ao J. (1999) observed a progressive decrease in surface area from 57 to 45 m²/g with 0.5 to 5.0% iron loading [37].

Z. Li et al. (2008) observed a smoother surface with Fe-doped TiO₂ nanoparticles, leading to decreased specific surface area [52] from 113 m²/g for undoped TiO₂ to 111 and 108 m²/g, respectively, for 1% and 5% Fe. Y. Zhang et al. (2021) reported reduced surface areas and porous volumes with >10% iron loading due to denser α-Fe₂O₃ nanoparticles occupying the interparticle voids of TiO₂ [61].

Adan C. (2006) stated that beyond 0.7%, excess iron segregates, occluding the pores and reducing their volume, average diameter, and surface area [22].

However, the surface area appears to be weakly dependent on iron, as shown in Figure 6.

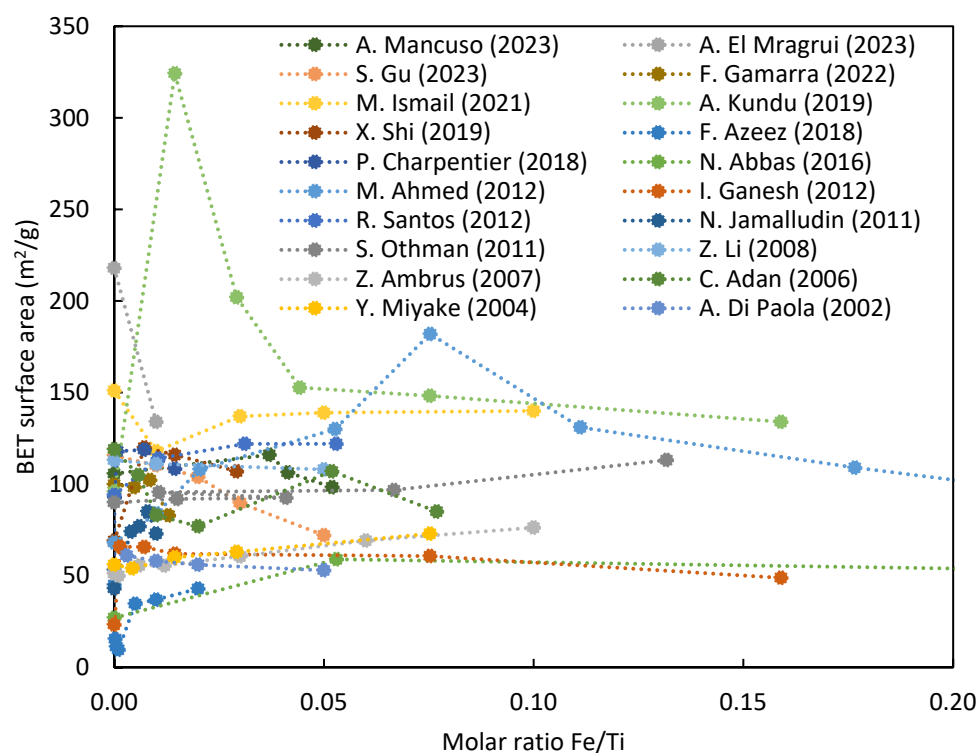


Figure 6. BET surface area of iron-doped TiO₂ nanoparticles at varying Fe/Ti ratio [22,31,51–54,56–59,62,71,74,84,86–92].

Iron has minimal impact on surface area beyond a threshold Fe/Ti ratio of 0.1, with only a slight decrease. Calcination temperature significantly affects surface area, necessitating control below 600 °C and iron concentration below 0.5% for optimal photocatalysts [93]. M. Qamar et al. (2014) found the highest photocatalytic activity at 450 °C, indicating a compromise between surface area and crystallinity [94]. M. Litter (1996) reported a similar result: decreasing surface area with increasing calcination temperature, emphasizing the need to control dopant concentration and optimize temperature between 450 and 600 °C for a large surface area (Figure 7).

The surface area decreased as the calcination temperature increased. Specifically, for the impregnation method, the surface area decreased from approximately 30 m²/g (at 500 °C) to 1 m²/g (at 1000 °C). A similar trend was observed for samples prepared using the co-precipitation method, albeit with less consistency in surface area due to different preparation methods. In contrast, the iron content, while introducing variations, did not significantly influence the surface area, except for iron contents between 0.5 and 2%. For instance, using the impregnation method, the surface area of the sample calcined at 650 °C decreased from 17 m²/g (with 0.5% iron content) to 9 m²/g (for the sample containing

5% iron). It is advisable to carefully control the dopant concentration, as an excess, likely above 0.5%, causes a moderate decrease in specific surface area due to pore occlusion. Furthermore, the optimal temperature for achieving a large surface area appears to be between 450 and 600 °C.

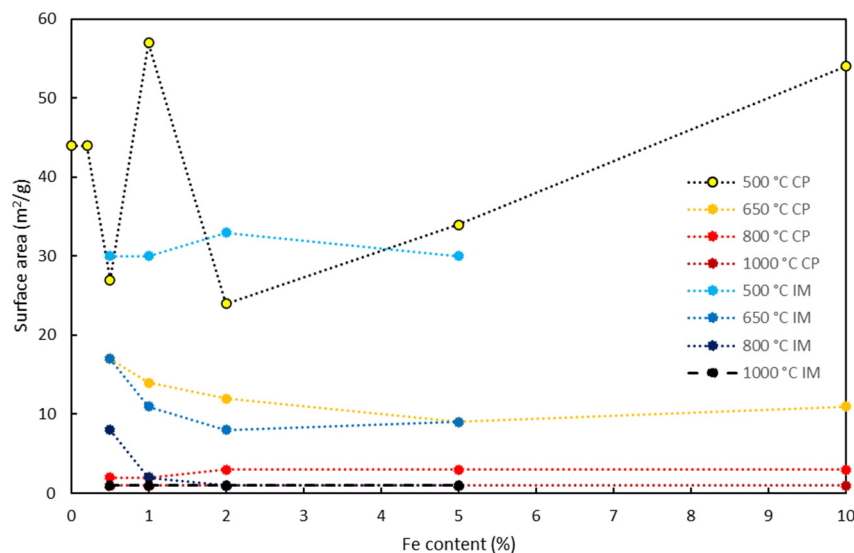


Figure 7. Surface area of Fe-doped titania samples prepared by impregnation (IM) and co-precipitation (CP) methods at different calcination temperatures [29].

3.4. Anatase to Rutile Transition

In addition to the calcination temperature, which promotes the formation of anatase beyond 370 °C [43] and the formation of rutile beyond 500 °C [79], considering the treatment time is crucial since the process is time-dependent, involving a reconstructive-type transformation [95,96]. Furthermore, iron is recognized as a promoter of rutile formation [97] more than other elements such as V and Cr [35]. This phenomenon is particularly evident when these elements are dissolved in a solid solution [29]. The rutile phase can be observed even at 400 °C during calcination when iron is present in high concentrations (>2% [43]).

The anatase phase is preferred for photocatalytic [7] and photovoltaic reactions due to its crystalline structure [41]. The higher band gap promotes the swift migration of charge carriers and inhibits positive hole–electron recombination [96]. This is owing to the specific structure with slightly greater distortion in the anatase phase compared to the rutile phase. In rutile, the energy level of the conduction band closely aligns with the reduction potential of O₂, delaying oxygen radicalization [10]. Additionally, anatase possesses a slightly higher Fermi level and a higher degree of surface hydroxylation compared to rutile, and its formation occurs at a lower temperature (T < 600 °C). This results in a larger available surface area for absorption and catalysis [98–100]. Furthermore, anatase is widely available and cost-effective. Therefore, iron could be perceived as an antagonist to photocatalysis.

Trivalent iron (Fe³⁺) induces oxygen vacancies to maintain local charge neutrality, given its lower oxidation state compared to Ti⁴⁺ in the titanium dioxide structure, promoting rutile formation, as commonly observed with ions having a smaller radius and lower valency than Ti⁴⁺ [46]. The presence of oxygen vacancies makes the material less “rigid” and more prone to reorganization of bonds towards thermodynamically more stable states, such as rutile [96].

Iron induces relaxation of the apical Ti–O bond in anatase, inhibiting the formation of surface Ti³⁺ due to its multi-valency. Transitioning between Fe²⁺ and Fe⁴⁺ can balance charge excesses, promoting the phase transition from anatase to rutile. The ability of iron to hinder the formation of surface Ti³⁺ and induce Ti–O bond relaxation facilitates

this transition. Elevated surface Ti^{3+} levels hinder the phase transition from anatase to rutile [28].

Furthermore, the multivalence of iron induces additional oxygen vacancies as it has the capability, during high-temperature calcination, to undergo reduction from Fe^{3+} to Fe^{2+} , causing the oxidation of oxygen to molecular oxygen. Experiments with Al^{3+} [28], having the same valency as Fe^{3+} and a similar ionic radius, lead to the inhibition of rutile formation. The use of Fe^{2+} also fails to promote rutile formation as it cannot induce oxygen vacancies in the titanium dioxide lattice [96].

Nasralla N. (2020) observed that, at the same calcination temperature (600 °C), the anatase phase was 17% with a 3% iron load but completely disappeared (quantitatively converting to rutile) at 8% iron load [41].

The significant role of iron and, notably, the decisive influence of the calcination temperature is evident in Figure 8. Notably, the specific duration of calcination, typically ranging from 1 to 4 h, has not been considered, except in the study by J. Navio (1998), where the sample was subjected to a 24-h treatment at 500 °C [37].

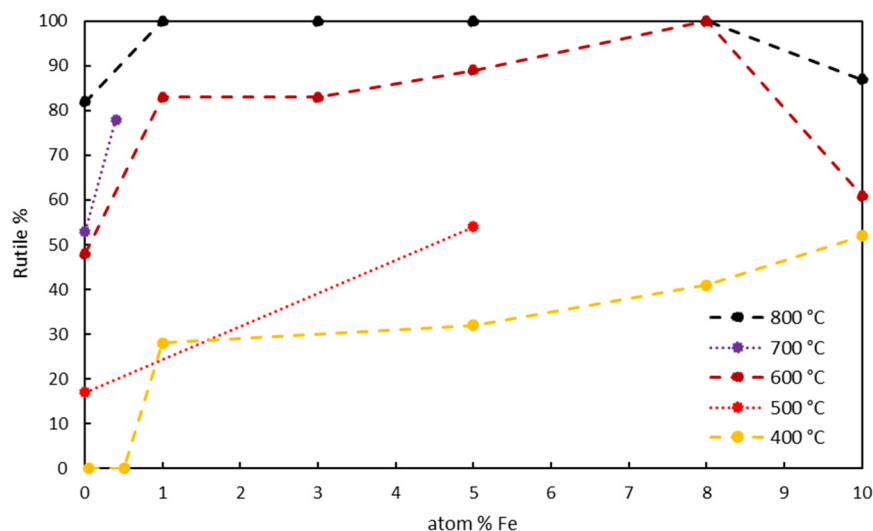


Figure 8. % of rutile phase in TiO_2 as a function of iron content and calcination temperature [37,41,43,101–104].

For excessive amounts of iron, the rutile phase decreases as non-negligible pseudo-brookite formation occurs [103] due to iron oxide segregation.

However, a mixture of anatase and rutile phases is optimal for photocatalytic processes compared to single-phase crystals [105,106]. The enhanced activity is due to the hetero-junction formation between different phases, efficiently separating spatial charges and, consequently, improving the TiO_2 quantum yield [107]. Given the slightly lower conduction band of rutile than anatase (approximately 0.2 eV), photogenerated electrons preferentially transfer from anatase to the rutile band, while positive holes follow the reverse process [21], leading to distinct photogenerated charges separation. Therefore, the mixture of anatase and rutile phases can effectively suppress the electrons and holes recombination, localizing them in rutile and anatase, respectively [41].

The intimate contact between the two phases is crucial to enhance the photocatalytic activity of mixed-phase TiO_2 [108]. Numerous studies have demonstrated that there exists an optimum ratio between the two phases of TiO_2 to maximize photocatalytic activity, highlighting the need to explore effective methods for synthesizing mixed-phase TiO_2 with close contact and a suitable ratio of the two phases [106].

Materials with a higher anatase/rutile ratio, typically 80:20, such as Degussa P25, a nanocrystalline material obtained through flame pyrolysis [96], exhibit superior photocatalytic activity [13,61]. A partial conversion towards rutile is desirable, even if induced by iron, as observed in a study by R. Bacsa (1998) where multiphase material of 70% anatase and 30% rutile showed enhanced performance [109].

High quantities of iron disrupt the octahedral structure of TiO₂ to such an extent that it leads to the formation of an amorphous phase in the overall material structure [35,81].

3.5. Charge Recombination

The trivalent iron (Fe³⁺) acts as a trap for both positive holes and photogenerated electrons, thereby increasing the lifetime of the photogenerated pair [52] and inhibiting their recombination [42]. Typically, the lifetime of photogenerated charges in titanium dioxide is around 200 microseconds [110], with the transfer of the photogenerated electron from TiO₂ to O₂ ranging from microseconds to milliseconds [44]. However, iron addition (0.5%) increases the lifetime to 50 milliseconds [63]. Higher charge carrier concentration induces a corresponding increase in photocatalytic reactivity [64], posing a crucial aspect in overcoming bottlenecks in photocatalytic processes [44]. Additionally, iron induces oxygen deficiencies [41] and undercoordinated titanium atoms in the TiO₂ structure, acting as an electron trap [28]. However, if an electron is trapped in a deep trapping site, it may have a longer lifetime but could also have a lower redox potential, potentially decreasing photocatalytic reactivity. The reactivity of doped TiO₂ appears to be complex, dependent on dopant concentration, the energy level of dopants within the TiO₂ lattice, their d-electronic configuration, the distribution of dopants, and the concentration of electron donors [110]. This effect is based on the presence of distinct energy levels resulting from the different oxidation states of iron (Fe⁴⁺/Fe³⁺) located above the valence band of TiO₂ and below the conduction band of pure TiO₂ [111].

During the initial step of the photocatalytic process, Fe²⁺ ions are produced as excess photogenerated electrons migrate from pure TiO₂ to Fe³⁺ [36]. Due to its instability arising from electron configuration loss (d⁵), Fe²⁺ swiftly oxidizes to Fe³⁺, transferring electrons to the adsorbed O₂ and forming superoxide ions [38,43]. Iron is an excellent electron acceptor compared to Ti⁴⁺, even for electrons released from the reverse process [36]. At the same time, Fe³⁺ can act as a trap for positive holes, considering its energy level (Fe³⁺/Fe⁴⁺) located above the valence band of TiO₂. Consequently, Fe⁴⁺ ions accept electrons and revert to Fe³⁺, while –OH groups transform into hydroxyl radicals. Bulk Fe³⁺ ions facilitate efficient charge separation by temporary electron trapping and extending the lifetime of positive holes, through surface–OH groups, producing hydroxyl radicals [36]. Charge carriers trapping (h⁺, e[−]) in different Fe³⁺ sites significantly enhance charge separation and interfacial charge transfer, thus enhancing photocatalytic efficiency [43].

However, beyond the optimal concentration, reported around 0.5% by W. Choi et al. (1994) [63] and 1% by Li X. (2003) [43], results in an exponential increase in the recombination rate. This is attributed to a decrease in the average distance between trapping sites due to the increasing number of dopants within the nanoparticle. The increased metal–metal interactions and energy transfer between nearby ions lead to the dominance of the concentration quenching process, becoming the predominant non-radiative decay process [41,47], reducing photocatalytic reactivity [38].

High iron loading induces additional phases, consequently, form a heterojunction between different phases [29]. This negatively impacts photocatalytic activity by increasing the recombination rate [32] and reducing charge mobility. Positive holes diffusing only 20–40 Å due to rapid recombination are particularly affected. Furthermore, in hematite, positive charges could be trapped in deep states such as Fe⁴⁺, significantly reducing their oxidizing power.

However, the heterojunction facilitates bidirectional charge transfer, leading to a distinct separation between positive holes and photogenerated electrons, reducing the charge recombination probability [18,61]. This occurs because the oxidation and reduction reactions take place separately in two different areas of the photocatalyst [8,21]. Specifically, electrons generated in the hematite conduction band migrate toward the TiO₂ conduction band, reacting with the adsorbed oxygen on the catalyst surface and producing the superoxide radical. Simultaneously, positive holes photogenerated in the TiO₂ valence band migrate towards the Fe₂O₃ valence band, reacting with adsorbed water to generate the

hydroxyl radical [112]. Therefore, the formation of a segregated iron oxide phase is not necessarily a negative phenomenon. It essentially represents a coupling between TiO_2 and iron oxide, a strategy widely used to enhance the photocatalytic performance of semiconductors by coupling them with semiconductors with a lower band gap, such as Fe_2O_3 , in this case (2.1 eV) [113]. An example is the study carried out previously [80], where selective leaching was performed on a titanium-based photocatalyst doped with iron to remove the segregated iron on the surface. The results showed a significant decrease in photocatalytic performance in the removal of rhodamine B.

3.6. pH_{ZC}

The pH of the environment significantly influences the overall efficiency of photocatalytic processes [98]. pH dependence can be associated with changes in the surface charge of the photocatalyst, hydrophobicity, net charge of pollutants, changes in adsorption modes, and the amount of produced hydroxyl radicals, thereby modifying the overall rate. Additionally, variations in pH may introduce deactivation problems if the presence of long-lived intermediates that inhibit the photocatalyst is favored [114]. The interaction of electron donors and acceptors with metal oxide semiconductors is influenced by surface chemistry and by the point of zero charge (pH_{ZC}), representing the pH value where the coverage of H^+ equals the coverage of OH^- . The pH_{ZC} is closely related to the surface acidity of a solid, and its knowledge allows for the evaluation of a surface propensity to become either positively or negatively charged as a function of pH, making it an essential parameter for defining or modulating the activity of a photocatalyst. Regarding TiO_2 , the principal amphoteric surface functionality is the “titanol” moiety, $-\text{TiOH}$. Hydroxyl groups on the TiO_2 surface are known to participate in an acid–base equilibrium, where pK_{a1} and pK_{a2} , constants of the first and second acid dissociation, at the pH_{ZC} for Degussa P25, the corresponding surface acidity constants were found to be 4.5 and 8.0 respectively, resulting in a pH_{ZC} of 6.25 [110,115]. This implies that interactions with cationic electron donors and electron acceptors will be favored at $\text{pH} > pH_{ZC}$ conditions, while anionic electron donors and acceptors will be favored at $\text{pH} < pH_{ZC}$ conditions [110]. Adsorption of relatively nonpolar pollutants, such as 1,2-diethyl phthalate, is enhanced at pH close to pH_{ZC} . On the other hand, the difference in pH_{ZC} values among various TiO_2 photocatalysts could affect the reaction mechanism. Furthermore, both the type and the amount of dopant metals influence this value [91]; the pH_{ZC} values of iron-containing titania increase significantly with the increase in metal content, indicating a surface enrichment of species with basic behavior such as iron oxides (hematite) and goethite. Iron modifies the photocatalyst pH_{ZC} , making it more basic [45]. For instance, A. Di Paola (2002) reported that the pH_{ZC} of titanium dioxide increased from 7.1 to 7.4 with 1% iron and further to 8.1 with 5% iron [91]. This implies that iron, by modifying the pH_{ZC} and subsequently altering the surface charge of the catalyst, can change the interaction between the catalyst surface and the target molecule. It can either promote or hinder the adsorption of the contaminant, thereby influencing the photocatalytic performance, significantly influenced by the adsorption step necessary for the target molecule to undergo photodegradation [36,116]. Hydroxyl radicals, due to their instability, have a short half-life, allowing them to diffuse only about 180 Å into the liquid bulk [117]. Therefore, they react only with molecules near the catalyst surface. The affinity of the target species towards the photocatalyst is crucial for effective photocatalytic degradation. This aligns with A. Di Paola (2004) observed that an increase in the amount of iron led to an increase in pH_{ZC} and, consequently, an increase in the interaction and degradation rate of formic acid. A similar effect for benzoic acid was observed, although steric hindrance led to interactions not solely dependent on pH_{ZC} . Due to acetic acid’s low acidity, a linear correlation between the surface basicity of the catalyst and the degradation of the target molecule was not observed [45].

3.7. Photocatalytic Performance

The photocatalytic performance is heavily influenced by the previously discussed parameters, which, in turn, are affected by the iron content. Establishing the dependence of photocatalysis on these parameters is very complex due to their interdependence and the various phenomena involved. Nevertheless, various authors have studied photocatalytic performance concerning iron content in the photocatalyst using widely varying reaction conditions and target molecules for degradation. For example, different irradiation employed, a parameter with a substantial influence on photocatalysis, complicates direct comparisons across studies [118]. Photocatalysis is also influenced by contaminant type and concentration, catalyst dosage, and solution turbidity. The solution pH can also impact the yield of the process; M. Nazari (2019) observed that at pH 4.5, the best-performing catalyst had 0.7 mol% Fe, while at pH 2.4, it was 3 mol% Fe [119].

Several authors agree on the optimal iron dosage that yields the best performance. For instance, Moradi H. (2016) reported that the optimal Fe³⁺ dosage for Reactive Red 198 degradation, in an investigation range between 0 and 10%, was 1%, attributing the performance decrease beyond this dosage to excessive recombination of photogenerated charges [6]. Ghorbanpour M. (2019) reported that the optimal performance in methyl orange degradation was achieved using a catalyst containing 0.5% Fe synthesized via the molten salt method [120]. Ochoa Rodriguez P. (2019) observed that for acid orange 7 degradation, the optimum was reached with 0.1% Fe [76]. The authors attributed these optimal performances to relatively low Fe/Ti ratios, ensuring that iron was finely dispersed in the crystal lattice of TiO₂.

In the phenol degradation, Adan C. (2006) observed that the best performance was achieved with an iron dosage in titania of 0.7–1%, corresponding to the maximum concentration of iron incorporable into the crystal lattice of titania without forming segregated phases of iron oxide [22]. Similarly, in the oxidation of cyclohexane, Li X. (2003) agrees on an optimal iron dosage of 1%, attributing the decrease in performance beyond this threshold to the formation of segregated iron oxide phases on the surface that deactivate active sites dedicated to photocatalytic degradation [43]. The deleterious effect of surface iron on photocatalytic activity was convincingly demonstrated by V. Moradi et al. (2019). Their research showcased that the removal of surface iron through selective leaching significantly enhanced the catalyst's efficiency in degrading phenol [121].

Furthermore, our previous study [80] has demonstrated, in contrast with V. Moradi, that surface-segregated iron was beneficial for enhancing photocatalytic performance. Specifically, removing the surface iron corresponding to approximately 10% of the total iron resulted in a decrease in the removal kinetics of rhodamine B, likely due to a reduced ability of the material to effectively separate photogenerated charges and prevent the recombination process, which is probably the rate-determining step under the employed conditions. This observation implies that the optimal amount of iron is contingent upon the specific contaminant. Consequently, the atom% of iron in TiO₂ corresponding to the maximum photocatalytic performance is documented in Table 1 through a comparative analysis of various studies.

Table 1 reveals a notable discrepancy among authors regarding the optimal iron dosage for methylene blue, ranging from 0.1 to 4.7%. In contrast, there is greater consensus for phenol and methyl orange, with optimal ranges of 0.1–0.6% and 0.1–0.5%, respectively. This observation holds interesting implications; varying iron dosages could potentially enable the synthesis of a selective photocatalyst tailored to a specific contaminant.

Table 1. Optimal atom% of Fe in TiO₂, leading to maximum degradation, varied with different contaminants. This analysis considered only systems exposed to visible radiation and where the optimal % was verified within the range of % iron explored, excluding extremes.

Contaminant	Atom% Fe	Reference
Methylene Blue	0.1	[65]
	0.1	[122]
	0.3	[118]
	0.7	[119]
	0.9	[48]
	2.7	[70]
	3.0	[123]
	4.7	[56]
Acid Orange 7	0.1	[76]
	3.7	[71]
Methyl Orange	0.1	[73]
	0.3	[124]
	0.5	[120]
Phenol	0.1	[125]
	0.5	[121]
	0.6	[22]
Cyclohexane	1.0	[43]
Direct Blue 119	4.2	[126]

Soria J. (1991) reported that in the reduction of molecular nitrogen for ammonia production, the most performing materials were found to have iron content of 0.2% and 0.5% [36]. In these materials, no surface-segregated iron was present. Therefore, the observed photocatalytic activity was mainly due to Fe³⁺ ions diffused in the crystal lattice of TiO₂. The decrease in activity with increasing surface enrichment in Fe suggests that surface iron negatively influences specific phases of the mechanism and/or specifically blocks certain surface sites. Since only non-surface Fe is active (Fe₂O₃ and Fe₂TiO₅), its role must be linked to the photogeneration and/or evolution of electrons and holes in TiO₂ grains. The observed influence of these iron ions in the photoreduction of dinitrogen can be explained by the hypothesis that they trap electrons, promoting their separation from the holes and allowing the latter to reach the surface. This, in turn, reacts with hydroxyl groups, giving rise to highly reactive hydroxyl radicals through surface chemical reactions. It is interesting to compare this result with the findings of Cordischi D. (1985), as they reached the same conclusions [34]. However, the most efficient material for ammonia production was found to have iron content of 0.5% and 1%. In this case, too, a decrease in photocatalytic performance was due to surface-segregated iron (Fe₂TiO₅). This concludes that surface-segregated iron negatively affects the process. However, the tendency to segregate depends on different synthesis conditions. Soria J. and D. Cordischi obtained different solubility limits, 0.5% for the former and 1% for the latter. However, Litter M. (1996) reported that the best performances related to the reduction of molecular nitrogen are achieved at iron dosages of 0.2% [29].

The consideration that the band gap decreases monotonically with increasing iron content up to a Fe/Ti molar ratio of 0.1 is noteworthy. This implies that lower band gaps do not necessarily correspond to better photocatalytic performance, suggesting the existence of other relevant phenomena.

To summarize, most authors analyzed in this review agree that surface-segregated iron oxide is detrimental to photocatalytic performance. Therefore, the optimal value of Fe to be employed often coincides with the maximum solubility limit in titanium oxide. However, it is important to emphasize that solubility, and thus the ability of titanium oxide to incorporate iron into the crystalline bulk, is closely dependent on the synthesis method employed, the calcination temperature, and the presence of anatase and rutile phases.

4. A Possible Optimized Synthesis of Nanoparticles Based on Iron-Doped TiO₂

Upon reviewing the scientific literature, a potentially optimized synthesis strategy for producing iron-doped titanium-based nanoparticles for photocatalytic treatments under visible light has been suggested. It was observed that the most suitable nanoparticle size ranged from 25 to 30 nm [49], achievable with an iron content of approximately 0.5%. This parameter appears independent of the synthesis strategy, although various methods were explored, with the majority employing the sol–gel method [50,55,127], followed by co-precipitation [128], hydrothermal [52], and solid-state methods [48].

The chosen synthesis strategy was found to potentially impact the solubility of iron, a critical factor in maximizing photocatalytic performance. Most authors identified the optimum point when the iron content in the titanium crystal lattice reached its maximum without forming segregated phases of iron oxides on the catalyst surface, which would compromise its activity [22,43]. Optimal performance was generally reported with iron content ranging from 0.5% to 1% [6,34,129], corresponding to the solubility of iron in anatase [42]. Exceptions, such as the study by Z. Wang (2001) and W. Teoh (2007) utilizing the spray pyrolysis strategy, demonstrated the possibility of achieving catalysts with 5–10% iron content without segregated phases [81], although performance was in line with other photocatalysis works (kinetic constant, $K = 0.36 \text{ h}^{-1}$) [27]. However, a precise comparison is challenging, given that reaction kinetics depend heavily on surrounding conditions, such as the light source used, the type of contaminant, and its concentration.

The impact of iron on surface area is minimal, with calcination temperature exerting a more pronounced influence [29]. Elevated calcination temperature leads to a decreased specific surface area. It is advisable to operate at relatively low temperatures, preferably above 370 °C, to facilitate anatase formation (the active phase of titanium) and below 500 °C to avoid excessive annealing processes and rutile formation. A desirable outcome involves a mixture of the two phases (20–30% rutile), proving more active than pure anatase [13,61]. Given that iron promotes the anatase–rutile transition and considering the time-dependent nature of the process, a recommended calcination temperature is approximately 450 °C [94] for 1–3 h.

Up to an iron content of 0.5–1.0%, the expected band gap is around 2.8 eV for 0.5% Fe and 2.7 eV for 1% Fe, suitable values for operation under visible light radiation. The precursor of iron and titanium does not seem to have relevance (for TiO₂, homemade production is preferable, as it is more easily dopable than Degussa P25 [48]).

Given the considerations and the fact that the synthesis of titania nanoparticles and doping with iron need not occur in two steps, a representative schematic of the proposed process has been illustrated in Figure 9.

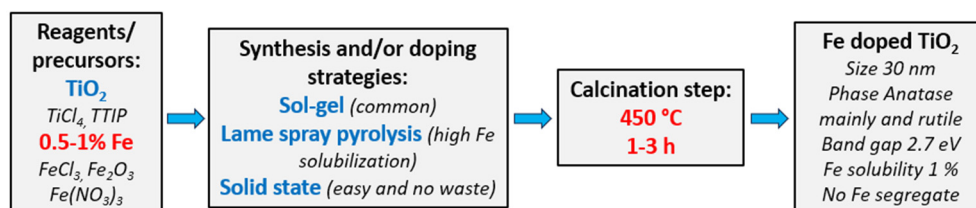


Figure 9. A possible optimized synthesis strategy to produce iron-doped titania nanoparticles for photocatalytic purposes.

For future commercial and research applications, especially in the water treatment field, it will be necessary not only to synthesize a high–performance photocatalyst in a simple and environmentally friendly manner able to operate under visible light but also to develop an effective strategy to immobilize the photocatalytic nanoparticles onto the surface of the supporting material [130,131] (to avoid costly phases of catalyst separation from the treated water [132,133]). It is worthwhile to investigate how efficacy varies with operating conditions, aiming to identify the optimal catalyst, whose properties can be modulated

based on the iron amount (or different dopants) used, depending on the effluent, conditions, and the target molecule, resulting in selective degradation. Additionally, it is essential to define accurate criteria for the selection of a photocatalytic reactor [134] with the optimal geometry necessary to provide effective irradiation [11].

5. Conclusions

The impact of iron on various parameters governing photocatalysis has been analyzed. It was observed that the presence of iron tends to reduce the nanoparticle size. However, beyond a threshold value, the reverse process occurs, as the initially spherical nanoparticles tend to elongate due to the rutile phase induced by iron. Indeed, iron serves as an excellent promoter of the anatase-to-rutile transition, detrimental for the material since the anatase phase is more photocatalytically active. However, a mix of the two phases is recommended to achieve superior performance.

Iron diminishes the band gap of the semiconductor from 3.1 eV to values comparable to hematite (1.9–2.1 eV), rendering the photocatalyst active even under visible light radiation. Specifically, up to Fe/Ti molar ratios of 0.1, the band gap consistently decreases with increasing iron content, settling around values of about 2.0 eV after surpassing this ratio of 0.1. Iron has the capability of extending the lifetime of the positively charged hole–electron pair, reducing the charge recombination rate, and consequently enhancing the material’s ability to produce hydroxyl radicals according to the photocatalytic mechanism.

Iron can alter the surface properties of titania by modifying the pH at the point of zero charge (pH_{ZC}), thereby influencing interactions between the photocatalyst surface and contaminants. Furthermore, it slightly alters the surface area at low dosages, while at high dosages, it tends to decrease due to the formation of surface-segregated iron oxide that occludes the material’s pores. Therefore, the formation of such segregated phases should be avoided, following the examined photocatalytic performances, which were found to be optimal around the maximum solubility limit of iron in the titania lattice, typically around 1%, depending on the synthesis strategy and conditions, especially calcination temperature.

In conclusion, a potential synthesis/doping strategy to optimize all the studied parameters has been proposed.

Author Contributions: Conceptualization, D.R. and N.A.; methodology, D.R.; validation, D.R. and L.D.P.; formal analysis, D.R.; investigation, D.R. and N.A.; data curation, D.R.; writing—review and editing, D.R., N.A. and L.D.P.; supervision, L.D.P. All authors have read and agreed to the published version of the manuscript.

Funding: This research received no external funding.

Data Availability Statement: The data presented in this study are available on request from the corresponding author.

Conflicts of Interest: The authors declare no conflicts of interest.

References

1. Mazzeo, L.; Rosa, D.; Bavasso, I.; Di Palma, L. Entrapped zinc oxide and titania nanoparticles in calcium alginate beads for the removal of Methylene Blue (MB): Adsorption properties and photocatalytic stability. *Chem. Eng. Trans.* **2021**, *84*, 181–186.
2. Ajmal, S.; Kumar, A.; Tabish, M.; Selvaraj, M.; Alam, M.M.; Mushtaq, M.A.; Zhao, J.; Owusu, K.A.; Saad, A.; Nazir, M.T.; et al. Modulating the microenvironment of single atom catalysts with tailored activity to benchmark the CO₂ reduction. *Mater. Today* **2023**, *67*, 203–228. [[CrossRef](#)]
3. Yasin, G.; Ali, S.; Ibraheem, S.; Kumar, A.; Tabish, M.; Mushtaq, M.A.; Ajmal, S.; Arif, M.; Khan, M.A.; Saad, A.; et al. Simultaneously Engineering the Synergistic-Effects and Coordination-Environment of Dual-Single-Atomic Iron/Cobalt-sites as a Bifunctional Oxygen Electrocatalyst for Rechargeable Zinc-Air Batteries. *ACS Catal.* **2023**, *13*, 2313–2325. [[CrossRef](#)]
4. Akerdi, A.G.; Bahrami, S.H. Application of heterogeneous nano-semiconductors for photocatalytic advanced oxidation of organic compounds: A review. *J. Environ. Chem. Eng.* **2019**, *7*, 103283. [[CrossRef](#)]
5. Zhao, W.; Chen, I.W.; Huang, F. Toward large-scale water treatment using nanomaterials. *Nano Today* **2019**, *27*, 11–27. [[CrossRef](#)]
6. Moradi, H.; Eshaghi, A.; Hosseini, S.R.; Ghani, K. Fabrication of Fe-doped TiO₂ nanoparticles and investigation of photocatalytic decolorization of reactive red 198 under visible light irradiation. *Ultrason Sonochem.* **2016**, *32*, 314–319. [[CrossRef](#)]

7. Mohseni-Salehi, M.S.; Taheri-Nassaj, E.; Hosseini-Zori, M. Effect of dopant (Co, Ni) concentration and hydroxyapatite compositing on photocatalytic activity of titania towards dye degradation. *J. Photochem. Photobiol. A Chem.* **2018**, *356*, 57–70. [[CrossRef](#)]
8. Malato, S.; Fernández-Ibáñez, P.; Maldonado, M.I.; Blanco, J.; Gernjak, W. Decontamination and disinfection of water by solar photocatalysis: Recent overview and trends. *Catal. Today* **2009**, *147*, 1–59. [[CrossRef](#)]
9. Tsang, C.H.A.; Li, K.; Zeng, Y.; Zhao, W.; Zhang, T.; Zhan, Y.; Xie, R.; Leung, D.Y.; Huang, H. Titanium oxide based photocatalytic materials development and their role of in the air pollutants degradation: Overview and forecast. *Environ. Int.* **2019**, *125*, 200–228. [[CrossRef](#)] [[PubMed](#)]
10. Padovese, E. Effetti di Strutturazione di Materiali a Base di Ossidi Inorganici di Tipo “aerogel-like” per Applicazioni nel Campo di Catalisi e di Isolanti ad alta Efficienza. Ph.D Thesis, Università degli studi di Trieste, Trieste, Italy, 2009.
11. Kusanov, Z.; Bakbolat, B.; Baimenov, A.; Issadykov, A.; Yeleuov, M.; Daulbayev, C. Photocatalysts for a sustainable future: Innovations in large-scale environmental and energy applications. *Sci. Total Environ.* **2023**, *885*, 163914. [[CrossRef](#)] [[PubMed](#)]
12. Likodimos, V. Advanced photocatalytic materials. *Materials* **2020**, *13*, 821. [[CrossRef](#)] [[PubMed](#)]
13. Velepini, T.; Prabakaran, E.; Pillay, K. Recent developments in the use of metal oxides for photocatalytic degradation of pharmaceutical pollutants in water—A review. *Mater. Today Chem.* **2021**, *19*, 100380. [[CrossRef](#)]
14. Alsheheri, S.Z. Nanocomposites containing titanium dioxide for environmental remediation. *Des. Monomers Polym.* **2021**, *24*, 22–45. [[CrossRef](#)] [[PubMed](#)]
15. Ding, Y.; Yang, I.S.; Li, Z.; Xia, X.; Lee, W.I.; Dai, S.; Bahnmann, D.W.; Pan, J.H. Nanoporous TiO₂ spheres with tailored textural properties: Controllable synthesis, formation mechanism, and photochemical applications. *Prog. Mater. Sci.* **2020**, *109*, 100620. [[CrossRef](#)]
16. Hasanuzzaman, M.; Islam, M.J.; Mokammel, M.A. Visible light induced self-cleaning performance of iron-doped TiO₂ nanoparticles for surface applications. *Int. J. Appl. Ceram. Technol.* **2023**. [[CrossRef](#)]
17. Lavand, A.B.; Malghe, Y.S.; Singh, S.H. Synthesis, Characterization, and Investigation of Visible Light Photocatalytic Activity of C Doped TiO₂/CdS Core-Shell Nanocomposite. *Indian J. Mater. Sci.* **2015**, *2015*, 690568. [[CrossRef](#)]
18. Kumaravel, V.; Mathew, S.; Bartlett, J.; Pillai, S.C. Photocatalytic hydrogen production using metal doped TiO₂: A review of recent advances. *Appl. Catal. B Environ.* **2019**, *244*, 1021–1064. [[CrossRef](#)]
19. Barba-Nieto, I.; Caudillo-Flores, U.; Fernández-García, M.; Kubacka, A. Sunlight-Operated TiO₂-Based Photocatalysts. *Molecules* **2020**, *25*, 4008. [[CrossRef](#)]
20. Rosa, D.; D’Agostino, F.; Bavasso, I.; Di Palma, L. An Innovative and Easy Method for Iron-doped Titania Synthesis. *Chem. Eng. Trans.* **2023**, *101*, 13–18.
21. Zu, M.; Zhou, X.; Zhang, S.; Qian, S.; Li, D.-S.; Liu, X.; Zhang, S. Sustainable engineering of TiO₂-based advanced oxidation technologies: From photocatalyst to application devices. *J. Mater. Sci. Technol.* **2021**, *78*, 202–222. [[CrossRef](#)]
22. Adán, C.; Bahamonde, A.; Fernández-García, M.; Martínez-Arias, A. Structure and activity of nanosized iron-doped anatase TiO₂ catalysts for phenol photocatalytic degradation. *Appl. Catal. B Environ.* **2006**, *72*, 11–17. [[CrossRef](#)]
23. Piera, E.; Tejedor-Tejedor, M.I.; Zorn, M.E.; Anderson, M.A. Relationship concerning the nature and concentration of Fe(III) species on the surface of TiO₂ particles and photocatalytic activity of the catalyst. *Appl. Catal. B Environ.* **2003**, *46*, 671–685. [[CrossRef](#)]
24. Tumbelaka, R.M.; Istiqomah, N.I.; Kato, T.; Oshima, D.; Suharyadi, E. High reusability of green-synthesized Fe₃O₄/TiO₂ photocatalyst nanoparticles for efficient degradation of methylene blue dye. *Mater. Today Commun.* **2022**, *33*, 104450. [[CrossRef](#)]
25. Abza, T.; Saka, A.; Tesfaye, J.L.; Gudata, L.; Nagaprasad, N.; Krishnaraj, R. Synthesis and Characterization of Iron Doped Titanium Dioxide (Fe: TiO₂) Nanoprecipitate at Different pH Values for Applications of Self-Cleaning Materials. *Adv. Mater. Sci. Eng.* **2022**, *2022*, 2748908. [[CrossRef](#)]
26. Jack, R.S.; Ayoko, G.A.; Adebajo, M.O.; Frost, R.L. A review of iron species for visible-light photocatalytic water purification. *Environ. Sci. Pollut. Res.* **2015**, *22*, 7439–7449. [[CrossRef](#)] [[PubMed](#)]
27. Teoh, W.Y.; Amal, R.; Mädler, L.; Pratsinis, S.E. Flame sprayed visible light-active Fe-TiO₂ for photomineralisation of oxalic acid. *Catal. Today* **2007**, *120*, 203–213. [[CrossRef](#)]
28. Vásquez, G.C.; Peche-Herrero, M.A.; Maestre, D.; Alemán, B.; Ramírez-Castellanos, J.; Cremades, A.; González-Calbet, J.M.; Piqueras, J. Influence of Fe and Al doping on the stabilization of the anatase phase in TiO₂ nanoparticles. *J. Mater. Chem. C Mater.* **2014**, *2*, 10377–10385. [[CrossRef](#)]
29. Litter, M.I.; Navio, J.A. Photocatalytic properties of iron-doped titania semiconductors. *J. Photochem. Photobiol. A Chem.* **1996**, *98*, 171–181. [[CrossRef](#)]
30. Afonso, C.; Lima, O.; Segundo, I.R.; Landi, S.; Margalho, É.; Homem, N.; Pereira, M.; Costa, M.F.M.; Freitas, E.; Carneiro, J. Effect of Iron-Doping on the Structure and Photocatalytic Activity of TiO₂ Nanoparticles. *Catalysts* **2023**, *13*, 58. [[CrossRef](#)]
31. Santos, R.d.S.; Faria, G.A.; Giles, C.; Leite, C.A.P.; Barbosa, H.d.S.; Arruda, M.A.Z.; Longo, C. Iron insertion and hematite segregation on Fe-doped TiO₂ nanoparticles obtained from sol-gel and hydrothermal methods. *ACS Appl. Mater. Interfaces* **2012**, *4*, 5555–5561. [[CrossRef](#)]
32. Fawzi Suleiman Khasawneh, O.; Palaniandy, P. Removal of organic pollutants from water by Fe₂O₃/TiO₂ based photocatalytic degradation: A review. *Environ. Technol. Innov.* **2021**, *21*, 101230. [[CrossRef](#)]
33. Kanjana, N.; Maiaugree, W.; Laokul, P. Photocatalytic activity of nanocrystalline Fe³⁺-doped anatase TiO₂ hollow spheres in a methylene blue solution under visible-light irradiation. *J. Mater. Sci. Mater. Electron.* **2022**, *33*, 4659–4680. [[CrossRef](#)]

34. Cordischi, D.; Burriesci, N.; D'Alba, F.; Petrer, S.M.; Polizzotti, G.; Schiavellos, M. Structural Characterization of Fe/Ti Oxide Photocatalysts by X-Ray, ESR, and Miissbauer Methods. *J. Solid State Chem.* **1985**, *56*, 182–190. [[CrossRef](#)]
35. Gracia, F.; Holgado, J.P.; Caballero, A.; Gonzalez-Elipe, A.R. Structural, optical, and photoelectrochemical properties of Mnⁿ⁺-TiO₂ model thin film photocatalysts. *J. Phys. Chem. B* **2004**, *108*, 17466–17476. [[CrossRef](#)]
36. Soria, J.; Conesa, J.C.; Augugliaro, V.; Palmisano, L.; Schiavello, M.; Sclafani, A. Dinitrogen Photoreduction to Ammonia over Titanium Dioxide Powders Doped with Ferric Ions. *J. Phys. Chem.* **1991**, *95*, 274–282. [[CrossRef](#)]
37. Naví, J.A.; Colón, G.; Maci, M.; Real, C.; Litter, M.I. Iron-doped titania semiconductor powders prepared by a sol±gel method. Part I: Synthesis and characterization. *Appl. Catal. A Gen.* **1999**, *177*, 111–120. [[CrossRef](#)]
38. Zhu, J.; Chen, F.; Zhang, J.; Chen, H.; Anpo, M. Fe³⁺-TiO₂ photocatalysts prepared by combining sol-gel method with hydrothermal treatment and their characterization. *J. Photochem. Photobiol. A Chem.* **2006**, *180*, 196–204. [[CrossRef](#)]
39. Navío, J.A.; Colon, G.; Trillas, M.; Peral, J.; Domenech, X.; Testa, J.J.; Padrón, J.; Rodri, D.; Litter, M.I. Heterogeneous photocatalytic reactions of nitrite oxidation and Cr(VI) reduction on iron-doped titania prepared by the wet impregnation method. *Appl. Catal. B Environ.* **1998**, *16*, 187–196. [[CrossRef](#)]
40. Zolfagharia, A.; Riazian, M.; Ashjari, M. Photodegradation of methylene blue and evans blue by iron and sulphur doped TiO₂ nanophotocatalyst under ultraviolet and visible light irradiation. *J. Mex. Chem. Soc.* **2021**, *65*, 357–375. [[CrossRef](#)]
41. Nasralla, N.H.S.; Yeganeh, M.; Šiller, L. Photoluminescence study of anatase and rutile structures of Fe-doped TiO₂ nanoparticles at different dopant concentrations. *Appl. Phys. A Mater. Sci. Process.* **2020**, *126*, 192. [[CrossRef](#)]
42. Zhang, Z.; Wang, C.C.; Zakaria, R.; Ying, J.Y. Role of Particle Size in Nanocrystalline TiO₂-Based Photocatalysts. *J. Phys. Chem. B* **1998**, *102*, 10871–10878. [[CrossRef](#)]
43. Li, X.; Yue, P.L.; Kutal, C. Synthesis and photocatalytic oxidation properties of iron doped titanium dioxide nanosemiconductor particles. *New J. Chem.* **2003**, *27*, 1264–1269. [[CrossRef](#)]
44. Ikeda, S.; Sugiyama, N.; Murakami, S.Y.; Kominami, H.; Kera, Y.; Noguchi, H.; Uosaki, K.; Torimoto, T.; Ohtani, B. Quantitative analysis of defective sites in titanium(IV) oxide photocatalyst powders. *Phys. Chem. Chem. Phys.* **2003**, *5*, 778–783. [[CrossRef](#)]
45. Di Paola, A.; García-López, E.; Marci, G.; Martín, C.; Palmisano, L.; Rives, V.; Venezia, A.M. Surface characterisation of metal ions loaded TiO₂ photocatalysts: Structure-activity relationship. *Appl. Catal. B Environ.* **2004**, *48*, 223–233. [[CrossRef](#)]
46. Loan, T.T.; Huong, V.H.; Huyen, N.T.; Van Quyet, L.; Bang, N.A.; Long, N.N. Anatase to rutile phase transformation of iron-doped titanium dioxide nanoparticles: The role of iron content. *Opt. Mater.* **2021**, *111*, 110651. [[CrossRef](#)]
47. Mwangi, I.W.; Kinyua, E.M.; Nthumbi, R.; Wanjau, R.N.; Swaleh, S.; Ngila, J.C. Iron (III) doped titanium dioxide coated dimensionally stable graphite anode electrode for electro-chemical treatment of domestic wastewater. *Heliyon* **2021**, *7*, e06671. [[CrossRef](#)] [[PubMed](#)]
48. Rosa, D.; D'Agostino, F.; Bavasso, I.; Bracciale, M.P.; Di Palma, L. Easy way to produce iron-doped titania nanoparticles via the solid-state method and investigation their photocatalytic activity. *J. Mater. Res.* **2023**, *38*, 1282–1292. [[CrossRef](#)]
49. Almquist, C.B.; Biswas, P. Role of synthesis method and particle size of nanostructured TiO₂ on its photoactivity. *J. Catal.* **2002**, *212*, 145–156. [[CrossRef](#)]
50. Luu, C.L.; Nguyen, Q.T.; Ho, S.T. Synthesis and characterization of Fe-doped TiO₂ photocatalyst by the sol-gel method. *Adv. Nat. Sci. Nanosci. Nanotechnol.* **2010**, *1*, 015008. [[CrossRef](#)]
51. Azeez, F.; Al-Hetlani, E.; Arafa, M.; Abdelmonem, Y.; Nazeer, A.A.; Amin, M.O.; Madkour, M. The effect of surface charge on photocatalytic degradation of methylene blue dye using chargeable titania nanoparticles. *Sci. Rep.* **2018**, *8*, 7104. [[CrossRef](#)] [[PubMed](#)]
52. Li, Z.; Shen, W.; He, W.; Zu, X. Effect of Fe-doped TiO₂ nanoparticle derived from modified hydrothermal process on the photocatalytic degradation performance on methylene blue. *J. Hazard. Mater.* **2008**, *155*, 590–594. [[CrossRef](#)] [[PubMed](#)]
53. Anwar Ismail, M.; Hedhili, M.N.; Anjum, D.H.; Singaravelu, V.; Ho Chung, S.; Zielinska-Jurek, A. Synthesis and Characterization of Iron-Doped TiO₂ Nanoparticles Using Ferrocene from Flame Spray Pyrolysis. *Catalysts* **2021**, *11*, 438. [[CrossRef](#)]
54. Ambrus, Z.; Balázs, N.; Alapi, T.; Wittmann, G.; Sipos, P.; Dombi, A.; Mogyorósi, K. Synthesis, structure and photocatalytic properties of Fe(III)-doped TiO₂ prepared from TiCl₃. *Appl. Catal. B Environ.* **2008**, *81*, 27–37. [[CrossRef](#)]
55. Crişan, M.; Răileanu, M.; Drăgan, N.; Crişan, D.; Ianculescu, A.; Niţoi, I.; Oancea, P.; Şomărescu, S.; Stănică, N.; Vasile, B.; et al. Sol-gel iron-doped TiO₂ nanopowders with photocatalytic activity. *Appl. Catal. A Gen.* **2015**, *504*, 130–142. [[CrossRef](#)]
56. Abbas, N.; Shao, G.N.; Haider, M.S.; Imran, S.M.; Park, S.S.; Kim, H.T. Sol-gel synthesis of TiO₂-Fe₂O₃ systems: Effects of Fe₂O₃ content and their photocatalytic properties. *J. Ind. Eng. Chem.* **2016**, *39*, 112–120. [[CrossRef](#)]
57. El Mragui, A.; Aadnan, I.; Zegaoui, O.; Esteves da Silva, J.C.G. Physico-chemical characterization and photocatalytic activity assessment under UV-A and visible-light irradiation of iron-doped TiO₂ nanoparticles. *Arab. J. Chem.* **2023**, *16*, 105331. [[CrossRef](#)]
58. Gamarra, F.; Medina, J.; Lanchipa, W.; Tamayo, R.; Sacari, E. Structural, Optical, and Arsenic Removal Properties of Sol-Gel Synthesized Fe-Doped TiO₂ Nanoparticles. *Nanomaterials* **2022**, *12*, 3402. [[CrossRef](#)] [[PubMed](#)]
59. Gu, S.; Zhang, W.; Wu, J.; Liu, X.; Liu, Z.; Xing, H.; Yu, L. Fabrication of iron doped titanium dioxide photocatalytic nanocomposite supported by water-quenched blast furnace slag and photocatalytic degradation of wastewater. *Ceram. Int.* **2023**. [[CrossRef](#)]
60. Egerton, T.A.; Harris, E.; Lawson, E.J.; Mile, B.; Rowlands, C.C. An EPR study of diffusion of iron into rutile. *Phys. Chem. Chem. Phys.* **2001**, *3*, 497–504. [[CrossRef](#)]

61. Zhang, Y.; Wu, L.; Wang, Y.; Zhang, Y.; Wang, H.; Wang, X.; Chen, X.D.; Wu, Z. Highly dispersed titania-supported iron oxide catalysts for efficient heterogeneous photo-Fenton oxidation: Influencing factors, synergistic effects and mechanism insight. *J. Colloid Interface Sci.* **2021**, *587*, 467–478. [[CrossRef](#)] [[PubMed](#)]
62. Ahmed, M.A.; El-Katori, E.E.; Gharni, Z.H. Photocatalytic degradation of methylene blue dye using Fe₂O₃/TiO₂ nanoparticles prepared by sol-gel method. *J. Alloys Compd.* **2013**, *553*, 19–29. [[CrossRef](#)]
63. Choi, W.; Termin, A.; Hoffmann, M.R. The Role of Metal Ion Dopants in Quantum-Sized TiO₂: Correlation between Photoreactivity and Charge Carrier Recombination Dynamics [Internet]. *J. Phys. Chem.* **1994**, *98*, 13669–13679. [[CrossRef](#)]
64. Husain, S.; Alkhtaby, L.A.; Giorgetti, E.; Zoppi, A.; Muniz Miranda, M. Investigation of the role of iron doping on the structural, optical and photoluminescence properties of sol-gel derived TiO₂ nanoparticles. *J. Lumin.* **2016**, *172*, 258–263. [[CrossRef](#)]
65. Sood, S.; Umar, A.; Mehta, S.K.; Kansal, S.K. Highly effective Fe-doped TiO₂ nanoparticles photocatalysts for visible-light driven photocatalytic degradation of toxic organic compounds. *J. Colloid Interface Sci.* **2015**, *450*, 213–223. [[CrossRef](#)] [[PubMed](#)]
66. Rahman, K.H.; Kar, A.K.; Chen, K.C.; Chen, C.J. Highly effective Fe-doped TiO₂ nanoparticles for removal of toxic organic dyes under visible light illumination. *Nanotechnology* **2023**, *34*, 245707. [[CrossRef](#)] [[PubMed](#)]
67. Vásquez, G.C.; Peche-Herrero, M.A.; Maestre, D.; Cremades, A.; Ramirez-Castellanos, J.; González-Calbet, J.M.; Piqueras, J. Effects of transition metal doping on the growth and properties of rutile TiO₂ nanoparticles. *J. Phys. Chem. C* **2013**, *117*, 1941–1947. [[CrossRef](#)]
68. Ramírez-Sánchez, I.M.; Bandala, E.R. Photocatalytic degradation of estriol using iron-doped TiO₂ under high and low UV irradiation. *Catalysts* **2018**, *8*, 625. [[CrossRef](#)]
69. Hung, W.C.; Fu, S.H.; Tseng, J.J.; Chu, H.; Ko, T.H. Study on photocatalytic degradation of gaseous dichloromethane using pure and iron ion-doped TiO₂ prepared by the sol-gel method. *Chemosphere* **2007**, *66*, 2142–2151. [[CrossRef](#)]
70. Komaraiah, D.; Radha, E.; Kalarikkal, N.; Sivakumar, J.; Ramana Reddy, M.V.; Sayanna, R. Structural, optical and photoluminescence studies of sol-gel synthesized pure and iron doped TiO₂ photocatalysts. *Ceram. Int.* **2019**, *45*, 25060–25068. [[CrossRef](#)]
71. Mancuso, A.; Sacco, O.; Vaiano, V.; Bonelli, B.; Esposito, S.; Freyria, F.S.; Blangetti, N.; Sannino, D. Visible light-driven photocatalytic activity and kinetics of Fe-doped TiO₂ prepared by a three-block copolymer templating approach. *Materials* **2021**, *14*, 3105. [[CrossRef](#)] [[PubMed](#)]
72. Solano, R.A.; Herrera, A.P.; Maestre, D.; Cremades, A. Fe-TiO₂ Nanoparticles Synthesized by Green Chemistry for Potential Application in Waste Water Photocatalytic Treatment. *J. Nanotechnol.* **2019**, *2019*, 4571848. [[CrossRef](#)]
73. Ismael, M. Enhanced photocatalytic hydrogen production and degradation of organic pollutants from Fe (III) doped TiO₂ nanoparticles. *J. Environ. Chem. Eng.* **2020**, *8*, 103676. [[CrossRef](#)]
74. Shi, X.; Zhang, Y.; Liu, X.; Jin, H.; Lv, H.; He, S.; Hao, H.; Li, C. A mild in-situ method to construct Fe-doped cauliflower-like rutile TiO₂ photocatalysts for degradation of organic dye in wastewater. *Catalysts* **2019**, *9*, 426. [[CrossRef](#)]
75. Mohan, H.; Ramasamy, M.; Ramalingam, V.; Natesan, K.; Duraisamy, M.; Venkatachalam, J.; Shin, T.; Seralathan, K.-K. Enhanced visible light-driven photocatalysis of iron-oxide/titania composite: Norfloxacin degradation mechanism and toxicity study. *J. Hazard. Mater.* **2021**, *412*, 125330. [[CrossRef](#)] [[PubMed](#)]
76. Ochoa Rodríguez, P.A.; Pecchi, G.A.; Casuscelli, S.G.; Elías, V.R.; Eimer, G.A. A simple synthesis way to obtain iron-doped TiO₂ nanoparticles as photocatalytic surfaces. *Chem. Phys. Lett.* **2019**, *732*, 136643. [[CrossRef](#)]
77. Anu Tharu, P.; Benoy, M.D.; Dhannia, T. Effect of annealing temperature on the bandgap of TiO₂ and Fe-doped titanium dioxide nanoparticles for enhancement of UV shielding performance. *Mater. Today Proc.* **2023**. [[CrossRef](#)]
78. Ellouzi, I.; Regraguy, B.; El Hajjaji, S.; Harir, M.; Schmitt-Kopplin, P.; Lachheb, H.; Laânab, L. Synthesis of Fe-doped TiO₂ with improved photocatalytic properties under Vis-L irradiation. *Iran. J. Catal.* **2022**, *12*, 283–293.
79. Bokhimi, X.; Morales, A.; Aguilar, M.; Toledo-Antonio, J.A.; Pedraza, F. Local order in titania polymorphs [Internet]. *Int. J. Hydrog. Energy* **2001**, *26*, 1279–1287. [[CrossRef](#)]
80. Rosa, D.; Lattanzio, S.; Bavasso, I.; Di Palma, L. Investigation of the synergistic effect of hydrogen peroxide and ultrasound on the photocatalytic treatment under visible light of dyes wastewater. *Chem. Eng. Sci.* **2023**, *282*, 119290. [[CrossRef](#)]
81. Wang, Z.M.; Yang, G.; Biswas, P.; Bresser, W.; Boolchand, P. Processing of iron-doped titania powders in flame aerosol reactors. *Powder Technol.* **2001**, *114*, 197–204. [[CrossRef](#)]
82. Babić, B.; Gulicovski, J.; Dohčević-Mitrović, Z.; Bučevac, D.; Prekajski, M.; Zagorac, J.; Matović, B. Synthesis and characterization of Fe³⁺ doped titanium dioxide nanopowders. *Ceram. Int.* **2012**, *38*, 635–640. [[CrossRef](#)]
83. Zhou, M.; Yu, J.; Cheng, B.; Yu, H. Preparation and photocatalytic activity of Fe-doped mesoporous titanium dioxide nanocrystalline photocatalysts. *Mater. Chem. Phys.* **2005**, *93*, 159–163. [[CrossRef](#)]
84. Jamalluddin, N.A.; Abdullah, A.Z. Reactive dye degradation by combined Fe(III)/TiO₂ catalyst and ultrasonic irradiation: Effect of Fe(III) loading and calcination temperature. *Ultrason. Sonochem.* **2011**, *18*, 669–678. [[CrossRef](#)] [[PubMed](#)]
85. Murashkina, A.A.; Murzin, P.D.; Rudakova, A.V.; Ryabchuk, V.K.; Emeline, A.V.; Bahnemann, D.W. Influence of the Dopant Concentration on the Photocatalytic Activity: Al-Doped TiO₂. *J. Phys. Chem. C* **2015**, *119*, 24695–24703. [[CrossRef](#)]
86. Ganesh, I.; Kumar, P.P.; Gupta, A.K.; Sekhar, P.S.; Radha, K.; Padmanabham, G.; Sundararajan, G. Processing and Application of Ceramics 6. *Sci. World J.* **2012**, *2012*, 127326. [[CrossRef](#)]
87. Kundu, A.; Mondal, A. Structural, optical, physio-chemical properties and photodegradation study of methylene blue using pure and iron-doped anatase titania nanoparticles under solar-light irradiation. *J. Mater. Sci. Mater. Electron.* **2019**, *30*, 3244–3256. [[CrossRef](#)]

88. Miyake, Y.; Tada, H. Photocatalytic Degradation of Methylene Blue with Metal-Doped Mesoporous Titania under Irradiation of White Light. *J. Chem. Eng. Jpn.* **2004**, *37*, 630–635. [[CrossRef](#)]
89. Charpentier, P.A.; Chen, C.; Azhie, K.; Grohe, B.; Mumin, M.A.; Lotus, A.F.; Therrien, P.; Mittler, S. Photocatalytic and antibacterial activities of silver and iron doped titania nanoparticles in solution and polyaspartic coatings. *Nanotechnology* **2019**, *30*, 085706. [[CrossRef](#)] [[PubMed](#)]
90. Abdul Rashid, S.; Othman, S.H.; Mohd Ghazi, T.I.; Abdullah, N. Fe-doped TiO₂ nanoparticles produced via MOCVD: Synthesis, characterization, and photocatalytic activity. *J. Nanomater.* **2011**, *2011*, 571601.
91. Di Paola, A.; Marci, G.; Palmisano, L.; Schiavello, M.; Uosaki, K.; Ikeda, S.; Ohtani, B. Preparation of polycrystalline TiO₂ photocatalysts impregnated with various transition metal ions: Characterization and photocatalytic activity for the degradation of 4-nitrophenol. *J. Phys. Chem. B* **2002**, *106*, 637–645. [[CrossRef](#)]
92. Mancuso, A.; Blangetti, N.; Sacco, O.; Freyria, F.S.; Bonelli, B.; Esposito, S.; Sannino, D.; Vaiano, V. Photocatalytic Degradation of Crystal Violet Dye under Visible Light by Fe-Doped TiO₂ Prepared by Reverse-Micelle Sol–Gel Method. *Nanomaterials* **2023**, *13*, 270. [[CrossRef](#)]
93. Wang, J.A.; Limas-Ballesteros, R.; López, T.; Moreno, A.; Gómez, R.; Novaro, O.; Bokhimi, X. Quantitative determination of titanium lattice defects and solid-state reaction mechanism in iron-doped TiO₂ photocatalysts. *J. Phys. Chem. B* **2001**, *105*, 9692–9698. [[CrossRef](#)]
94. Qamar, M.; Merzougui, B.; Anjum, D.; Hakeem, A.S.; Yamani, Z.H.; Bahnemann, D. Synthesis and photocatalytic activity of mesoporous nanocrystalline Fe-doped titanium dioxide. *Catal. Today* **2014**, *230*, 158–165. [[CrossRef](#)]
95. Rosa, D.; Cimini, G.; Bracciale, M.P.; Felici, A.C.; Di Palma, L. Iron-doped titania nanoparticles supported on polystyrene for photocatalytic treatment of contaminated water in a continuous system. *J. Photochem. Photobiol. A Chem.* **2024**, *447*, 115241. [[CrossRef](#)]
96. Hanaor, D.A.H.; Sorrell, C.C. Review of the anatase to rutile phase transformation. *J. Mater. Sci.* **2011**, *46*, 855–874. [[CrossRef](#)]
97. Long, Y.; Luo, X.; Zhang, L.; Xue, X.; Yin, Y.; Zhu, Z.; Xu, B. High-temperature transformation behavior of iron-doped titanium dioxide crystal structures. *Phase Transit.* **2021**, *94*, 219–235. [[CrossRef](#)]
98. Carp, O.; Huisman, C.L.; Reller, A. Photoinduced reactivity of titanium dioxide. *Prog. Solid State Chem.* **2004**, *32*, 33–177. [[CrossRef](#)]
99. Thomas, A.G.; Flavell, W.R.; Mallick, A.K.; Kumarasinghe, A.R.; Tsoutsou, D.; Khan, N.; Chatwin, C.; Rayner, S.; Smith, G.C.; Stockbauer, R.L.; et al. Comparison of the electronic structure of anatase and rutile TiO₂ single-crystal surfaces using resonant photoemission and x-ray absorption spectroscopy. *Phys. Rev. B* **2007**, *75*, 035105. [[CrossRef](#)]
100. Tanaka, K.; Capule, M.F.; Hisanaga, T. Effect of crystallinity of TiO₂ on its photocatalytic action. *Chem. Phys. Lett.* **1991**, *187*, 73–76. [[CrossRef](#)]
101. Kissoum, Y.; Mekki, D.E.; Bououdina, M.; Sakher, E.; Bellucci, S. Dependence of Fe Doping and Milling on TiO₂ Phase Transformation: Optical and Magnetic Studies. *J. Supercond. Nov. Magn.* **2020**, *33*, 427–440. [[CrossRef](#)]
102. Nasralla, N.; Yeganeh, M.; Astuti, Y.; Piticharoenphun, S.; Shahtahmasebi, N.; Kompany, A.; Karimipour, M.; Mendis, B.G.; Poolton, N.R.J.; Šiller, L. Structural and spectroscopic study of Fe-doped TiO₂ nanoparticles prepared by sol-gel method. *Sci. Iran* **2013**, *20*, 1018–1022.
103. Nasralla, N.H.S.; Yeganeh, M.; Astuti, Y.; Piticharoenphun, S.; Šiller, L. Systematic study of electronic properties of Fe-doped TiO₂ nanoparticles by X-ray photoemission spectroscopy. *J. Mater. Sci. Mater. Electron.* **2018**, *29*, 17956–17966. [[CrossRef](#)]
104. Faycal Atitar, M.; Ismail, A.A.; Al-Sayari, S.A.; Bahnemann, D.; Afanasev, D.; Emeline, A.V. Mesoporous TiO₂ nanocrystals as efficient photocatalysts: Impact of calcination temperature and phase transformation on photocatalytic performance. *Chem. Eng. J.* **2015**, *264*, 417–424. [[CrossRef](#)]
105. Kawahara, T.; Konishi, Y.; Tada, H.; Tohge, N.; Nishii, J.; Ito, S. A Patterned TiO₂ (Anatase)/TiO₂ (Rutile) Bilayer-Type Photocatalyst: Effect of the Anatase/Rutile Junction on the Photocatalytic Activity. *Angew. Chem. Int. Ed.* **2002**, *41*, 2935–2937. [[CrossRef](#)]
106. Tian, B.; Li, C.; Zhang, J. One-step preparation, characterization and visible-light photocatalytic activity of Cr-doped TiO₂ with anatase and rutile bicrystalline phases. *Chem. Eng. J.* **2012**, *191*, 402–409. [[CrossRef](#)]
107. Romero-Gomez, P.; Borrás, A.; Barranco, A.; Espinos, J.P.; Gonzalez-Eliphe, A.R. Enhanced photoactivity in bilayer films with buried rutile-anatase heterojunctions. *ChemPhysChem* **2011**, *12*, 191–196. [[CrossRef](#)]
108. Li, G.; Gray, K.A. Preparation of mixed-phase titanium dioxide nanocomposites via solvothermal processing. *Chem. Mater.* **2007**, *19*, 1143–1146. [[CrossRef](#)]
109. Bacsá, R.R.; Kiwi, J. Effect of rutile phase on the photocatalytic properties of nanocrystalline titania during the degradation of p-coumaric acid. *Appl. Catal. B Environ.* **1998**, *16*, 19–29. [[CrossRef](#)]
110. Hoffmann, M.R.; Martin, S.T.; Choi, W.; Bahnemann, D.W. Environmental Applications of Semiconductor Photocatalysis. *Chem. Rev.* **1995**, *95*, 69–96. [[CrossRef](#)]
111. Niu, Y.; Xing, M.; Zhang, J.; Tian, B. Visible light activated sulfur and iron co-doped TiO₂ photocatalyst for the photocatalytic degradation of phenol. *Catal. Today* **2013**, *201*, 159–166. [[CrossRef](#)]
112. Khasawneh, O.F.S.; Palaniandy, P.; Palaniandy, P.; Ahmadipour, M.; Mohammadi, H.; Bin Hamdan, M.R. Removal of acetaminophen using Fe₂O₃-TiO₂ nanocomposites by photocatalysis under simulated solar irradiation: Optimization study. *J. Environ. Chem. Eng.* **2021**, *9*, 104921. [[CrossRef](#)]

113. Wodka, D.; Socha, R.P.; Bielańska, E.; Elźbieciak-Wodka, M.; Nowak, P.; Warszyński, P. Photocatalytic activity of titanium dioxide modified by Fe₂O₃ nanoparticles. *Appl. Surf. Sci.* **2014**, *319*, 173–180. [[CrossRef](#)]
114. Chen, J.; Eberlein, L.; Langford, C.H. Pathways of phenol and benzene photooxidation using TiO₂ supported on a zeolite. *J. Photochem. Photobiol. A Chem.* **2002**, *148*, 183–189. [[CrossRef](#)]
115. Kormann, C.; Bahnemann, D.W.; Hoffmann, M.R. Photolysis of Chloroform and Other Organic Molecules in Aqueous TiO₂ Suspensions [Internet]. *Environ. Sci. Technol.* **1991**, *25*, 494–500. [[CrossRef](#)]
116. Isari, A.A.; Payan, A.; Fattahi, M.; Jorfi, S.; Kakavandi, B. Photocatalytic degradation of rhodamine B and real textile wastewater using Fe-doped TiO₂ anchored on reduced graphene oxide (Fe-TiO₂/rGO): Characterization and feasibility, mechanism and pathway studies. *Appl. Surf. Sci.* **2018**, *462*, 549–564. [[CrossRef](#)]
117. Hashemzadeh, F.; Rahimi, R.; Ghaffarinejad, A.; Hashemzadeh, F.; Rahimi, R.; Gaffarinejad, A. Photocatalytic Degradation of Methylene blue and Rhodamine B dyes by Niobium Oxide Nanoparticles synthesized Via Hydrothermal method [Internet]. *Int. J. Appl. Chem. Sci. Res.* **2013**, *1*, 95–102.
118. Su, B.; Wang, K.; Bai, J.; Mu, H.; Tong, Y.; Min, S.; She, S.; Lei, Z. Photocatalytic degradation of methylene blue on Fe³⁺-doped TiO₂ nanoparticles under visible light irradiation. *Front. Chem. China* **2007**, *2*, 364–368. [[CrossRef](#)]
119. Nazari, M. Iron-doped Titanium Dioxide Nanomaterials: Synthesis, Characterization and Photodegradation Catalytic Behavior. Ph.D. Thesis, York University, Toronto, ON, Canada, 2019.
120. Ghorbanpour, M.; Feizi, A. Iron-doped TiO₂ Catalysts with Photocatalytic Activity. *J. Water Environ. Nanotechnol.* **2019**, *4*, 60–66.
121. Moradi, V.; Ahmed, F.; Jun, M.B.G.; Blackburn, A.; Herring, R.A. Acid-treated Fe-doped TiO₂ as a high performance photocatalyst used for degradation of phenol under visible light irradiation. *J. Environ. Sci.* **2019**, *83*, 183–194. [[CrossRef](#)]
122. Lin, W.C.; Liu, R.; Yang, W.D. Effect of iron (III)-doping on the photocatalytic activity of titanium dioxide catalysts for methylene blue degradation. *Appl. Mech. Mater.* **2012**, *117–119*, 1088–1091. [[CrossRef](#)]
123. Ali, T.; Tripathi, P.; Azam, A.; Raza, W.; Ahmed, A.S.; Ahmed, A.; Muneer, M. Photocatalytic performance of Fe-doped TiO₂ nanoparticles under visible-light irradiation. *Mater. Res. Express. Inst. Phys. Publ.* **2017**, *4*, 015022. [[CrossRef](#)]
124. Xia, Z.; Xing, S.; Wang, H.; Zhao, D.; Wu, S.; Jiang, W.; Wang, N.; Liu, S.; Liu, C.; Ding, W.; et al. Weak-visible-light-driven Fe doped TiO₂ photocatalyst prepared by coprecipitation method and degradation of methyl orange. *Opt. Mater.* **2022**, *129*, 112522. [[CrossRef](#)]
125. Jamil, T.S.; Gad-Allah, T.A.; Ghaly, M.Y. Parametric study on phenol photocatalytic degradation under pure visible and solar irradiations by Fe-doped TiO₂. *Desalination Water Treat.* **2012**, *50*, 264–271. [[CrossRef](#)]
126. Saroj, S.; Singh, L.; Singh, S.V. Photodegradation of Direct Blue-199 in carpet industry wastewater using iron-doped TiO₂ nanoparticles and regenerated photocatalyst. *Int. J. Chem. Kinet.* **2019**, *51*, 189–205. [[CrossRef](#)]
127. Bokov, D.; Turki Jalil, A.; Chupradit, S.; Suksatan, W.; Javed Ansari, M.; Shewael, I.H.; Valiev, G.H.; Kianfar, E. Nanomaterial by Sol-Gel Method: Synthesis and Application. *Adv. Mater. Sci. Eng.* **2021**, *2021*, 5102014. [[CrossRef](#)]
128. Li, R.; Jia, Y.; Bu, N.; Wu, J.; Zhen, Q. Photocatalytic degradation of methyl blue using Fe₂O₃/TiO₂ composite ceramics. *J. Alloys Compd.* **2015**, *643*, 88–93. [[CrossRef](#)]
129. Liu, T. Preparation of modified TiO₂ and its photocatalytic properties. *Acad. J. Mater. Chem.* **2023**, *4*, 1–14.
130. Gelover, S.; Mondragón, P.; Jiménez, A. Titanium dioxide sol-gel deposited over glass and its application as a photocatalyst for water decontamination. *J. Photochem. Photobiol. A Chem.* **2004**, *165*, 241–246. [[CrossRef](#)]
131. Mansilla, H.; Bravo, C.; Ferreyra, R.; Litter, M.; Jardim, W.; Lizama, C.; Freer, J.; Fernández, J. Photocatalytic EDTA degradation on suspended and immobilized TiO₂. *J. Photochem. Photobiol. A Chem.* **2006**, *181*, 188–194. [[CrossRef](#)]
132. Shan, A.Y.; Ghazi, T.I.M.; Rashid, S.A. Immobilisation of titanium dioxide onto supporting materials in heterogeneous photocatalysis: A review. *Appl. Catal. A Gen.* **2010**, *389*, 1–8. [[CrossRef](#)]
133. Bideau, M.; Claudel, B.; Dubien, C.; Faure, L.; Kazouan, H. On the “immobilization” of titanium dioxide in the photocatalytic oxidation of spent waters. *J. Photochem. Photobiol. A Chem.* **1995**, *91*, 137–144. [[CrossRef](#)]
134. Prakruthi, K.; Ujwal, M.P.; Yashas, S.R.; Mahesh, B.; Kumara Swamy, N.; Shivvaraju, H.P. Recent advances in photocatalytic remediation of emerging organic pollutants using semiconducting metal oxides: An overview. In *Environmental Science and Pollution Research*; Springer Science and Business Media Deutschland GmbH: Berlin, Germany, 2022; Volume 29, pp. 4930–4957.

Disclaimer/Publisher’s Note: The statements, opinions and data contained in all publications are solely those of the individual author(s) and contributor(s) and not of MDPI and/or the editor(s). MDPI and/or the editor(s) disclaim responsibility for any injury to people or property resulting from any ideas, methods, instructions or products referred to in the content.